Accurate Rendering of Liquid-Crystals and Inhomogeneous Optically Anisotropic Media

SHLOMI STEINBERG, University of California, Santa Barbara

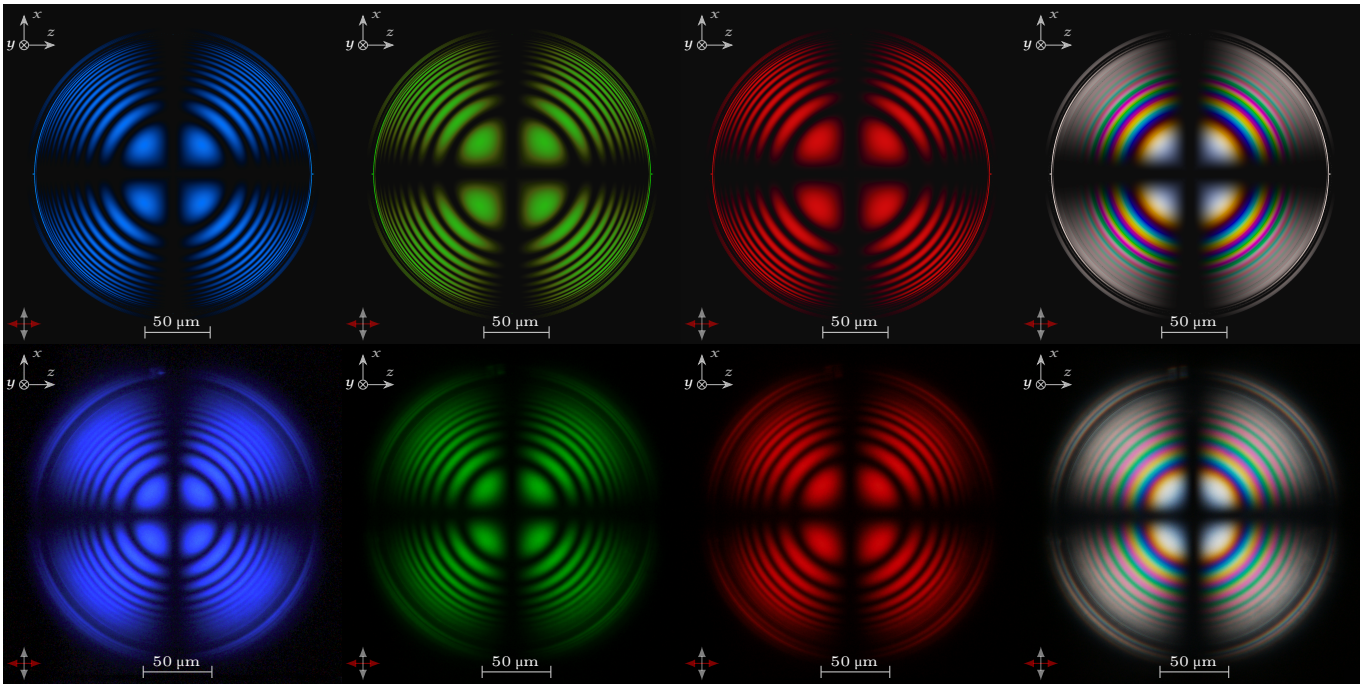

Fig. 1. Comparison of liquid-crystal shells rendered using our method (top) and polarized microscopy photos (micrographs) of similar liquid-crystal shells (bottom). The shells are formed when a spherical liquid-crystal droplet suspended in liquid is injected with an optically isotropic liquid (see figure 9 for an illustration of the geometry). The imaging is performed by passing linearly polarized light, emitted from a source at $-y$, through the shell and then through a polarizer oriented perpendicular to the source polarization ("cross polarized" light) and finally captured by a camera located at $+y$. The orientation of the polarizers is depicted in the bottom left corner of the figures. The shells were illuminated using blue ($480\,\mathrm{nm}$), green ($580\,\mathrm{nm}$), red ($630\,\mathrm{nm}$) and white (illuminant E) light. The artefacts around the left and right edges of the rendered shells are numerical errors. See subsection 5.1 for a more in-depth discussion. The polarized microscopy photos (bottom) were adapted from "Transmission polarized optical microscopy of short-pitch cholesteric liquid crystal shells", in Emerging Liquid Crystal Technologies XI, by Geng, Y., Noh, J., and Lagerwall, J.P.F., ©2016 [Geng et al. 2016], reproduced with permission.

We present a novel method for devising a closed-form analytic expression to the light transport through the bulk of inhomogeneous optically anisotropic media. Those optically anisotropic materials, e.g., liquid-crystals and elastic fluids, arise in a plethora of established applications and exciting new research, however current state-of-the-art methods of visually deducing their optical properties or rendering their appearance are either lacking or non-existent. We formulate our light transport problem under the context of electromagnetism and derive, from first principles, a differential equation of the transmitted complex wave fields that fully account for the complicated interference phenomena that arise. At the core of our proposed rendering framework is a powerful mathematical representation, carefully crafted to enable us to produce highly accurate analytic approximative solutions for the light transport. This approach is previously unused in computer rendering, and our framework is capable of accurately rendering optically anisotropic materials with spatially varying optical properties at orders-of-magnitude better performance compared to existing methods. We demonstrate a few practical applications of our method and we validate it against polarized photos of liquid-crystals as well as numerically against numerical solvers and qualitatively against brute-force renderings.

CCS Concepts: • **Computing methodologies** → **Rendering**; • **Applied computing** → *Physics*.

Additional Key Words and Phrases: wave optics, polarized imaging, light transport, physical and mathematical representation

ACM Reference Format:
Shlomi Steinberg. 2020. Accurate Rendering of Liquid-Crystals and Inhomogeneous Optically Anisotropic Media. *ACM Trans. Graph.* 39, 3, Article 22 (April 2020), 23 pages. https://doi.org/10.1145/3381748

Author's address: Shlomi Steinberg, p@shlomisteinberg.com, University of California, Santa Barbara, Santa Barbara, California, 93106.

© 2020 Copyright held by the owner/author(s). Publication rights licensed to ACM. This is the author's version of the work. It is posted here for your personal use. Not for redistribution. The definitive Version of Record was published in *ACM Transactions on Graphics*, https://doi.org/10.1145/3381748.

1 INTRODUCTION

Optical anisotropy is the property of matter where electromagnetic radiation (such as light) propagates with different phase velocities depending on its polarization plane in that medium. This optical property gives rise to what is known as *Birefringence*—sometimes referred to as "double refraction"—where an electromagnetic wave that refracts into an anisotropic material is split into two waves of different velocities depending on the incident wave's polarization. Birefringence is source to a multitude of optical phenomena unique to optically anisotropic materials.

In this paper our focus is on modelling and rendering the light transport that happens in the bulk of those refractive, translucent, inhomogeneous, birefringent materials. The term "inhomogeneous" is used to refer to materials which exhibit continuously varying optical properties, such as the refractive-indices, as opposed to materials that give rise to scattering by particles. Actually, scattering is ignored in our light transport formulation as it is often negligible and does not contribute to the fringe patterns that characterize the visual appearance of those materials. Our rendering framework could be considered as an "anisotropic wave-optics" version of the Refractive Radiative Transfer Equation [Ament et al. 2014], with the main difference being that our framework deals with double refraction and the resulting wave interference.

The fringe patterns that arise due to those wave interference phenomena are difficult to predict. Indeed, a highly complex behaviour emerges when light propagates in such media: Due to the spatially varying optical properties light keeps refracting into additional wavefronts (or "rays", using geometric-optics terminology), which results in infinitely many wavefronts, essentially a field of amplitudes, all of which potentially interfere with each other. The analysis of those patterns and the phase shift differentials that shape them is known as *anisotropic interferometry* and is of interest for a broad range of current and emerging applications and research, such as a variety of liquid-crystal display (LCD) devices, spatial light modulators, polarized-phase microscopy, organizing nanoparticles, tunable liquid-crystal devices and elastic turbulence. However, the difficulty of experimental realization of theoretical predictions of the optical behaviours is a common problem [Ricardez-Vargas and Volke-Sepúlveda 2010] and existing methodology mostly relies on costly and time consuming experimental methods. Likewise the inverse problem of deducing optical properties from polarized images remains a difficult obstacle and an area of active research [Wu et al. 2016].

The primary contribution of this paper is a rendering framework that addresses the problem of accurately rendering such materials at interactive performance, a problem virtually ignored by current research. Due to the complex nature of the problem, tracing rays in such media is inadequate for the task of fully capturing the coherent light transport, instead we account for the entire field of amplitudes that arises. To that end, we use the electromagnetic wave theory to formulate the light transport, under a few relaxations, as an operator-valued differential equation and then present a mathematical representation method, unseen so-far in computer graphics, to devise an accurate analytic approximant for this light transport equation.

This approach serves to create a rendering framework that accurately captures the visual appearance of liquid-crystals under different configurations, as well as other anisotropic materials as they appear under polarized imaging. Our presented framework is capable of rendering surfaces of different topologies, like liquid-crystal droplets, microdroplets, shells and cells of arbitrary diameters and sizes, under incident monochromatic light of any polarization, intensity and at any incidence angle.

We limit the rest of our discussion to liquid-crystals as they provide an encompassing working example of an inhomogeneous optically anisotropic medium. In addition, they are ubiquitous in practical applications and designing and predicting a liquid-crystal's optical properties and molecular orientation remains an open problem.

1.1 Motivation

The difficulty of deduction and elucidation of a liquid-crystal cell's mesoscopic structures and optical properties is well studied. The process is oft done by visual inspection with polarised imaging devices, or via a more rigorous approach that relies on costly experimental setup [Bennis et al. 2017; Guo et al. 2016; Ogiwara et al. 2007]. Additional techniques, like state-of-the-art PolScope-based methods [Shribak 2011; Shribak and Oldenbourg 2003] aim to produce a 2D spatial linear retardance map, however the provided insight into the structure of highly inhomogeneous media, like liquid-crystals, is limited. Interactive accurate rendering of those materials would allow us to perform "inverse rendering", where information about the optical properties can be deduced from image measurements.

In recent years research has also turned to the realm of machine learning in attempts to employ neural networks to classify images and deduce optical properties from polarized micrographs: Walters et al. [2019] explore the possibility of using neural networks to classify topological defects in liquid-crystals, but their training and test datasets were synthetically produced by a Monte-Carlo simulation and do not resemble (nor aim to) realistic micrographs. Doi et al. [2019] employ neural networks to aid in local structure analysis of liquid crystal polymers and Smith et al. [2020] study the use of convolutional neural networks to extract information from micrographs and conclude that better simulation methods are required. Datasets remain limited and expensive to generate, which hampers the development of similar methods [Cao et al. 2018]. Our rendering framework can be used to generate synthetic, but realistic and accurate (see figure 1), datasets.

Furthermore, just as deducing a liquid-crystal's structure from micrographs is difficult, so is the inverse problem of predicting the optical response given a specific optical configuration. Nonetheless this problem is also of great interest: Fabrication and design of liquid-crystals cells with predetermined optical behaviour remains at the heart of a vast array, too numerous to exhaustively list, of modern and future applications in the field of applied materials, e.g., for bio-sensing [Lee et al. 2015], "smart" windows [Kim et al. 2015] or adaptive lens [Kaur et al. 2016]. However, the deduction of the correct chemical composition, or the required intensity of the applied electric field, is currently done via slow experimental data acquisition and analysis.

Interferometry is also used in non-contact applications (due to risk factors, or practical considerations), such as medical applications in live tissue analysis [Bavigadda et al. 2012]. As biological tissues tend to exhibit birefringence under some conditions (due to photoelasticity), medical imaging is also a potential application of our method.

Finally, our method also has applications in the study of the visualization of liquid-crystals [Callan-Jones et al. 2006; Čopar et al. 2013].

2 RELATED WORK

The electromagnetic theory concerning optical anisotropy is well known and has been extensively studied for decades, yet tracing rays in such media is still an area of active research, while the problem of rendering the visual phenomena that arise in optically anisotropic materials that exhibit inhomogeneity in their optical properties has largely been ignored. Our derivation builds upon existing optical principles, yet we go beyond tracing individual rays nor do we discretise our medium into layers. Instead, we formulate the problem as a differential initial value problem in order to account for its continuous nature. Media that exhibit continuously spatially varying optical properties are sometimes referred to as "non-linear" (not to be confused with non-linear optics), and previous work has attempted to derive the radiative transfer through the bulk of such materials: Gantri [2014] describes an iterative computational framework that employs the Legendre transform method to approximate the radiative transfer. There has also been attempts to render media with linearly varying refractive-indices via an analytic solution to the ray equation and application thereof to photon mapping [Cao et al. 2010]; to perform relighting of refractive objects [Sun et al. 2008] or caustics-aware dynamic volume illumination [Magnus and Bruckner 2018] by adjusting the ray-marching step in accordance with the gradient of the varying refractive-index; to render fire effects [Pegoraro and Parker 2006]; to extend photon mapping to non-linear volumes [Gutierrez et al. 2008]; to render ray-traced images of gradient-index spherical or cylindrical lenses [Suffern and Getto 1991]; and to ray-trace by using the eikonal equation to model a medium with a spatially varying refractive-index [Stam and Languénou 1996]. Finally, the Refractive RTE (Radiative Transfer Equation) [Ament et al. 2014] presents a framework for rendering participating media with a varying refractive-index. However, all those works are performed under the context of the simpler and more common isotropic optics, and thus far no work has attempted to derive a fast and accurate light transport framework for optically anisotropic media with continuously varying optical properties that accounts for wave interference.

On the other hand, there is a small body of work that contemplates the rendering of optically anisotropic materials with constant optical properties. Tannenbaum et al. [1994]; Weidlich and Wilkie [2008] render double refractions in polarized ray traced renderers while Latorre et al. [2012] aims to render double refractions of biaxial media by pre-computing a lookup table. An analytic formulation for the spectral integral of the iridescence that arises in an optically anisotropic homogeneous slab is presented by Steinberg [2019]. Zhdanov et al. [2019] present another ray tracing method in anisotropic media of partially polarized light represented via the Stokes-Müller formalism. An intriguing approach to depth imaging by positioning a crystal in front of a camera lens was introduced by Baek et al. [2016]. Nevertheless, all those approaches essentially discuss geometric ray-tracing in optically anisotropic media, and as those formalisms are discrete they are ill-suited for considering the entire amplitude field that arises when the medium's optical properties vary spatially.

Propagation in inhomogeneous optically anisotropic media. Existing research that deals with light propagation in stratified optically anisotropic media is mostly based on Berreman's 4×4 matrix method [Berreman 1972], where an operator differential equation is derived from Maxwell's equations. The 4x4 matrix method has given rise to a large body of research, where interference effects are generally ignored, the derivations are constrained or are mostly suitable for numerical work [Aslanyan et al. 2015; D. Tentori 2008; Eidner et al. 1989; Stallinga 1999]. We reformulate the problem and use a different mathematical approach to solve the differential equation, fully accounting for interference induced by the entire field of amplitudes. Additional research extracts the eigenmodes supported by a metamaterial consisting of a twisted stack of periodic layers [Askarpour et al. 2014], and investigates the colour shift in liquid-crystal cells of uniform twist [De Meyere 1994]. Kolomiets [2013] studies the polarization states in inhomogeneous non-depolarizing media with elliptical phase anisotropy via an application of the differential Jones and Müller matrices.

Geometric ray-tracing and multi-layered formalisms. Additional research relating to inhomogeneous anisotropic media has been largely confined to geometric tracing of a singular ray, in particular via an application of the Hamiltonian method for uniaxial [Sluijter et al. 2008] and biaxial [Sluijter et al. 2009] media, and later extended to arbitrary coordinate systems [Akbarzadeh and Danner 2010]. Kravtsov et al. [2007] use Müller calculus to derive the evolution equation for Stokes vectors in a weakly anisotropic smoothly inhomogeneous medium.

Other research employs multi-layered models: Nishidate [2013] considers an inhomogeneous layered system where the optic axis is fixed and performs the calculations in the principal coordinate frame. Further work derives analytic formulations for transmission and reflection in matrix form in a multi-layered structure [Kiasat et al. 2014; Simonenko 2010], and discusses propagation in a twisted nematic liquid-crystal cell modelled as a stack of anisotropic layers [Youn et al. 2014]. Those methods were later used to develop a GP-GPU solution for tracing in inhomogeneous anisotropic media [Guerreiro et al. 2017]. Postava et al. [2002] classify layers in a multi-layered anisotropic structure into thin, and therefore optically coherent, and thick, ergo incoherent, layers. Another relevant work predicts an inhomogeneous thin-film's bidirectional scattering distribution function (BSDF) in Müller matrix form using the distorted-wave Born approximation [Germer et al. 2017]. Katsidis and Siapkas [2002] introduce coherence-transformation matrices, directly related to Müller matrices, in order to model incoherent propagation between homogeneous layers. Jakob et al. [2014] presents a general framework for deriving the BSDFs of arbitrary layered materials.

Additional related work in the realm of computer graphics. Computer graphics research that discusses polarized light transport and wave optics has also been inspirational: Jarabo and Arellano [2018]; Mojzík et al. [2016] have also used the Müller calculus for polarization aware bidirectional ray tracing. Polarization under subsurface scattering was discussed by Collin et al. [2014], who pre-computes a tabulated bidirectional reflectance distribution function (BRDF) by solving the vector radiative transport equation. The optical coherence of an ensemble of light waves was considered for construction of high-resolution BRDFs [Levin et al. 2013] and for the rendering of physically accurate diffractions induced by arbitrary surfaces [Cuypers et al. 2012; Toisoul and Ghosh 2017; Werner et al. 2017; Yan et al. 2018]. Finally, Bar et al. [2019] use a well-known result in optics, which states that speckle fields are an instance of a multivariate Gaussian distribution, to device a Monte-Carlo simulation of coherent light transport for the purpose of rendering speckle fields.

3 PROPAGATION IN STRATIFIED INHOMOGENEOUS ANISOTROPIC MEDIA

In this section we model and formalise our problem domain. Our physical model consists of a *stratified medium*, that is a medium that can be modelled as an infinite plane-parallel slab where the optical properties vary continuously but only along the depth of the slab. A stratified slab can be thought of as a stack of infinitely many infinitesimally thin slices. Note that we do not limit ourselves to any form of a "layered" (in the traditional sense) model and indeed the optical properties in our model are described by continuous functions. Nor are we limited to materials where the optical properties only vary spatially along the depth of the material, this is due to the fact that different functions can be used each time we sample the analytic approximation to the light transport (usually at each rendered pixel), and because the footprint on the surface of the material that participates in the light transport is generally on the orders of magnitude smaller than the pixel size. Finally, we are also not restricted to a slab model in practice: As the participating footprint on the surface of the slab is small, any smooth surface geometry can be approximated very well by a plane in the footprint's region, that is our surface geometry is a piece-wise linear structure with very small simplexes. Those claims will be empirically demonstrated when we discuss results in section 5.

We begin by providing a short background concerning the relevant optical theory of anisotropic optics. The curious reader is referred to Bloss [1961]; Born and Wolf [1999] for a far more comprehensive discussion of optical anisotropy or to Steinberg [2019] where a very simple derivation of the relevant quantities is provided.

3.1 Background: Optical Anisotropy

The permittivity $\hat{\epsilon} = \epsilon + i\sigma$ in an optically isotropic medium is a (possibly complex) scalar, where the complex part, σ, is the medium's conductivity. Birefringence arises when anisotropy is induced in the electric susceptibility and the permittivity becomes a symmetric rank 2 tensor [Born and Wolf 1999], in which case the medium is described as optically anisotropic. Given the eigenvalues (also known as *principal permittivities*) of the permittivity tensor, denoted $\hat{\epsilon}_{1,2,3} = \epsilon_{1,2,3} + i\sigma_{1,2,3}$, optically anisotropic media can be classified into two categories:

- *Uniaxial*, where two of the eigenvalues are identical; and
- *biaxial*, where all the permittivities are distinct.

For simplicity and practicality (as most liquid-crystals are uniaxial) our discussion is limited to uniaxial media. We denote the eigenvalue with multiplicity 2 as the *ordinary permittivity*, $\hat{\epsilon}_o = \epsilon_o + i\sigma_o$, and the eigenvalue with multiplicity 1 as the *extraordinary permittivity*, $\hat{\epsilon}_e = \epsilon_e + i\sigma_e$. The material's ordinary and extraordinary indices-of-refraction are then

$$\eta_o = \sqrt{\hat{\epsilon}_o} \qquad \eta_e = \sqrt{\hat{\epsilon}_e} \tag{1}$$

The permittivity tensor's eigenvectors are called the *principal axes* of the material, and the eigenvector associated with the extraordinary permittivity is the distinguished direction known as the *optic axis*, denoted $\vec{\mathrm{a}}$. No polarity arises in the optic axis, i.e. $\pm\vec{\mathrm{a}}$ are physically equivalent.

SYMBOLS	
$\hat{\epsilon}_{o,e}$	Ordinary and extraordinary complex permittivities
$\eta_{o,e}$	Ordinary and extraordinary refractive-indices
$\kappa_{o,e}$	Ordinary and extraordinary absorption coefficients
$\phi_{o,e}$	Ordinary and extraordinary phases
$\Delta\phi$	Phase shift
λ	Wave length
$\langle\vec{\mathrm{a}},\vec{\mathrm{b}}\rangle$	Inner product between $\vec{\mathrm{a}}$ and $\vec{\mathrm{b}}$
$\mathcal{T}_n$	Taylor expansion operator (of order n)
$\mathfrak{e}$	Error function that quantifies the accuracy of our method
$\mathbf{\Phi}_{\Delta y}(y)$	Phase progression operator for propagation from y to $y+\Delta y$
$\varsigma_{\Delta y}(y)$	Absorption operator for propagation from y to $y+\Delta y$
$\boldsymbol{\mathcal{A}}$	The 2×2 complex operator of the light transport ODE
$\boldsymbol{\mathcal{P}}_{\Delta y}(y)$	Propagation operator from y to $y+\Delta y$
$\boldsymbol{\mathcal{T}}_{\Delta y}(y)$	Transmission operator for propagation from y to $y+\Delta y$
T_{in}	Transmission matrix into the medium
$\mathrm{T}_{\mathrm{out}}$	Transmission matrix out of the medium
ψ	2-dimensional complex Jones vector
τ	Thickness of rendered material
$\vec{\mathrm{a}}$	Optic axis of an anisotropic medium
$\vec{\mathrm{k}}$	Wavevector
$\vec{\mathrm{s}}$	Wave's phase velocity direction (i.e. wavefront's direction)
e^{Ω}	The 2×2 complex operator that is the solution to the light transport ODE
f, g_1, g_2, g_3	Scalar complex functions that decompose e^{Ω}
K	Incidence parameter
k	Wavenumber
$t_{\xi\zeta}$	Fresnel transmission coefficient from a ξ-wave to a ζ-wave (ξ,ζ can be o, e, s or p)
$U(\mathrm{p},t)$	Plane wave, as a function of position and time

Table 1: List of symbols

The material equations that supplement Maxwell's equations describe the relation between the electric field vector $\vec{\mathrm{E}}$ and the electric displacement vector $\vec{\mathrm{D}}$, viz. $\vec{\mathrm{D}} = \hat{\epsilon}\vec{\mathrm{E}}$, and a direct consequence of the permittivity being a tensor is that $\vec{\mathrm{E}}$ and $\vec{\mathrm{D}}$ of a wave propagating in an optically anisotropic medium no longer coincide [Born and Wolf 1999]. This divergence gives rise to birefringence, where an electromagnetic wave perceives different permittivity values depending on the direction of its electric field. Waves in anisotropic media are then classified as either *ordinary waves*, which always perceive the ordinary permittivity $\hat{\epsilon}_o$, or *extraordinary waves*, with *effective permittivity* $\hat{\epsilon}_{\mathrm{ef}}$ (see appendix C for an explicit equation) being a value between $\hat{\epsilon}_o$ and $\hat{\epsilon}_e$. The difference in phase velocities causes the wavevectors—which describe a wavefront's direction and spatial frequency—denoted $\vec{\mathrm{k}}_{o,e}$, to diverge as well. We further denote $\vec{\mathrm{s}}$ to be the phase velocity direction of a wavefront:

$$\vec{\mathrm{s}}_o = \frac{\vec{\mathrm{k}}_o}{\left|\vec{\mathrm{k}}_o\right|} \qquad \vec{\mathrm{s}}_e = \frac{\vec{\mathrm{k}}_e}{\left|\vec{\mathrm{k}}_e\right|} \tag{2}$$

See figure 2 for an illustration of the propagation in an homogeneous anisotropic cell. It is worth noting that the law of reflection and Snell's law of refraction, as they are known in the context of isotropic optics, do not apply to the extraordinary wave.

A medium's *degree-of-birefringence* is defined as

$$\Delta\eta = \eta_e - \eta_o \tag{3}$$

and is used to quantify how birefringent a medium is: Greater values of $|\Delta\eta|$ result in larger divergence between $\vec{\mathrm{k}}_o$ and $\vec{\mathrm{k}}_e$. When $\Delta\eta > 0$ (positive birefringence) the ordinary wave has a higher phase velocity and vice versa under negative birefringence.

Sources of anisotropy. Optical anisotropy can arise via a variety of reasons, for example:

- Solid crystals of non-cubic lattice systems are common birefringent materials and the anisotropy arises naturally due to the crystal's lattice structure.
- Photoelasticity is optical anisotropy induced by elastic deformations due to mechanical forces.
- Induced by electro-optical effects via an application of an external electric or magnetic field.
- Molecular structure can give rise to birefringence, with liquid-crystals being a prime example.
- Metamaterials where small structural properties causes birefringence, e.g., different carbon-metal flakes.

as well as other more exotic sources. Our focus is on liquid-crystals, where the *director field*—the spatial configuration of the optic axis—has the unique property of taking different shapes and forms due to different surface anchoring and can change dynamically by an introduction of an external electric field and/or flow. Inhomogeneity isn't limited to the optic axis but arises in addition in the permittivities, e.g., due to a temperature gradient (see section 5.2).

The explicit equations for the electric fields, wavevectors and the effective index-of-refraction as perceived by a propagating wave, are given in appendix C. Finally, the Fresnel transmission and reflection coefficients dictate the amplitude ratios between participating waves at an interface between a couple of media. The Fresnel coefficients equations for isotropic-anisotropic, anisotropic-isotropic and anisotropic-anisotropic interfaces are available in our supplemental material.

While our focus is on uniaxial materials, the rest of the paper is also applicable, in theory, to biaxial materials (where $\hat{\epsilon}_1 \neq \hat{\epsilon}_2 \neq \hat{\epsilon}_3 \neq \hat{\epsilon}_1$) as well.

3.2 Light Propagation in Stratified Inhomogeneous Anisotropic Media

Stratified inhomogeneous slab. We consider the following geometry (see figure 2): A plane-parallel, horizontally infinite, optically anisotropic slab of constant thickness τ, surrounded by a homogeneous, isotropic medium. Without loss of generality, our coordinate system is chosen such that one of the interfaces (denoted the "upper" interface) coincides with the xz-plane ($y \equiv 0$), the y-axis coincides with the slab's normal vector and therefore the "lower" interface is positioned at $y \equiv -\tau$.

As discussed, the slab is modelled as a stratified inhomogeneous medium, that is a vertical stack of homogeneous slabs, and the inhomogeneity is then only y-dependant. We start by considering the discrete case, where each layer in the stack is of thickness $\Delta y > 0$. For simplicity we assume that the slab's ordinary permittivity is constant and the inhomogeneity arises in the extraordinary permittivity and the optic axis only. $\epsilon_e(y)$, $\sigma_e(y)$ and $\vec{\mathrm{a}}(y)$ are then functions of y, and we restrict those to be real analytic on an open set D, such that $[0, -\tau] \subset D$. Then, the optical properties of the n-th slab in the vertical stack, positioned at

$$-n\Delta y \leq y < -(n-1)\Delta y$$

are given by $\hat{\epsilon}_e(-n\Delta y)$ and $\vec{\mathrm{a}}(-n\Delta y)$, as well as the constant $\hat{\epsilon}_o$. In practice the assumptions of isotropy and homogeneity of the surrounding medium are superfluous as is the assumption that the slab's ordinary permittivity is constant. It would be simple to eliminate those constraints, however we choose to retain them for the sake of the discussion's clarity.

Transmission into and out of the slab. Let U be a monochromatic plane-wave of wavelength λ propagating in the upper medium, $y > 0$ (depicted in blue in figure 2):

$$U(\mathrm{p}, t) = U_0 e^{i\left(\langle\vec{\mathrm{k}},\mathrm{p}\rangle - \omega t + \varphi\right)} \tag{4}$$

with $\vec{\mathrm{k}}$ being the wavevector, U_0 the peak magnitude, ω the angular frequency, φ the phase shift, t the time variable and p the position. For the rest of the discussion we ignore the concept of time and fix t. We also define the *wavenumber* as $k = |\vec{\mathrm{k}}| = \frac{2\pi}{\lambda}$. Without loss of generality we also assume that $\vec{\mathrm{k}}$ resides in the yz-plane, denoted as the *incidence plane*. Let $\langle\vec{\mathrm{k}}, \mathrm{p}\rangle = c_0$, for some constant c_0, be a wavefront of U that intersects the upper interface and refracts into the slab at $z = z_0$. Then the complex amplitude of the incident light can be expressed by a *Jones vector*, a complex two-dimensional vector which describes fully coherent light. The incident Jones vector

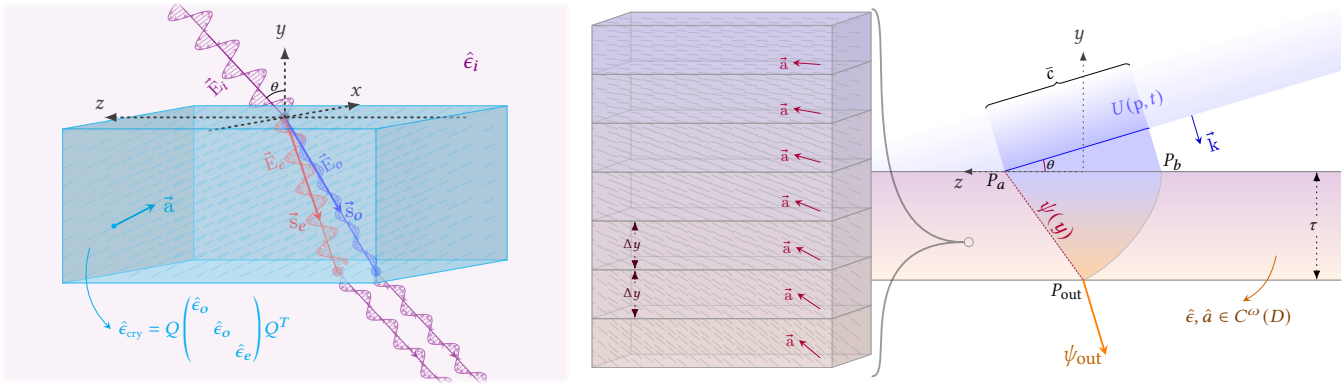

(a) Homogeneous uniaxial crystal cell (b) Stratified slab (c) Propagation in inhomogeneous media

Fig. 2. (a) Illustration of light refracting through an homogeneous uniaxial crystal. The splitting of the incident wavefront into ordinary (blue) and extra-ordinary (red) wavefronts is demonstrated. Note that while the permittivity of the surrounding medium, $\hat{\epsilon}_i$, is a scalar, the crystal's permittivity, $\hat{\epsilon}_{\text{cry}}$, is a rank 2 symmetric tensor that gives rise to the ordinary and extraordinary refractive-indices once diagonalized. The direction of the optic axis of the crystal, $\vec{a}$, is illustrated as well via short cyan spikes throughout the medium. (b) A discrete stack of homogeneous slabs, each of thickness Δy and with distinct optical properties, is known as a *stratified* medium. (c) When $\Delta y \to 0$ the discrete stack becomes a continuous inhomogeneous slab of thickness τ, where the permittivity and optic axis are now y-dependant functions analytic in some open interval D such that $[0, -\tau] \subset D$. A plane wave $U(p,t)$, incident at angle θ, is depicted in blue. Note that as the system is not discrete a continuous region of length $\bar{c}$ of the incident wavefront (highlighted in blue) participates in the radiative transfer through the bulk of the medium (highlighted in a violet-to-orange gradient). Finally, the exitant radiation ψ_{out} is depicted in orange.

at point $\mathrm{p}_a = [\,0{,}0{,}z_0\,]^T$ is then

$$\hat{\psi}\Big|_{\mathrm{p}_a} = \begin{bmatrix} \hat{\psi}_s \\ \hat{\psi}_p \end{bmatrix}\Big|_{\mathrm{p}_a} = \begin{bmatrix} U_s(\mathrm{p}_a) \\ U_p(\mathrm{p}_a) \end{bmatrix} \tag{5}$$

where $U_{s,p}$ are the complex amplitudes of the incident plane-wave projected onto the incidence plane (s-polarized) and onto the plane spanned by the wavevector $\vec{k}$ and the x-axis (p-polarized), respectively. To express the amplitudes of the ordinary and extraordinary waves, that arise once the incident wave is refracted into the slab, we keep using complex two-dimensional vectors, which are sometimes called "*extended Jones vectors*" [Yeh 1982]. The subtle distinction is that while ("common") Jones vectors are typically used to describe the orthogonal amplitudes of a wave, the wavevectors of ordinary and extraordinary waves, $\vec{s}_o$ and $\vec{s}_e$, do not coincide in general nor are their electric fields perpendicular. However in practice this distinction is of no import, as the ordinary and extraordinary waves are intrinsically related, and as the notation is identical we drop the "extended" moniker. Then, the amplitudes immediately after refraction are

$$\psi\Big|_{\mathrm{p}_a} = \begin{bmatrix} \psi_o \\ \psi_e \end{bmatrix}\Big|_{\mathrm{p}_a} = \mathrm{T}_{\text{in}} \cdot \hat{\psi}\Big|_{\mathrm{p}_a} \qquad \mathrm{T}_{\text{in}} = \begin{bmatrix} \hat{t}_{so} & \hat{t}_{po} \\ \hat{t}_{se} & \hat{t}_{pe} \end{bmatrix} \tag{6}$$

with T_{in} being the transmission matrix from the incident wave to the first layer ($y \in [-\Delta y, 0]$) of the stratified slab. The first subscript of each of the Fresnel coefficients $\hat{t}$ indicates the type of source wave and the second subscript the type of destination wave, e.g., $\hat{t}_{se}$ is the Fresnel coefficient for an s-polarized source wave to an extraordinary destination wave.

As $\hat{\epsilon}_o$ is identical for all layers, by assumption, the wavevectors $\vec{s}_o$ remains constant as well. Therefore the ordinary wavefronts have the same direction of propagation in all layers. Then, for convenience and without loss of generality, we choose the exit point p_{out} as the intersection between the lower interface ($y \equiv -\tau$) and the ray in direction $\vec{s}_o$ from point p_a (the path $\mathrm{p}_a\mathrm{p}_{\text{out}}$ in figure 2) and set z_0 such that p_{out} lies on the y-axis.

Our problem statement is then to find an analytic expression for $\psi\big|_{\mathrm{p}_{\text{out}}}$, in which case the final solution would then be

$$\psi_{\text{out}} = \mathrm{T}_{\text{out}} \cdot \psi\Big|_{\mathrm{p}_{\text{out}}} \qquad \mathrm{T}_{\text{out}} = \begin{bmatrix} t_{os} & t_{es} \\ t_{op} & t_{ep} \end{bmatrix} \tag{7}$$

where T_{out} is analogous to T_{in} and its Fresnel coefficients relate the relevant amplitudes with the last layer of the slab as the source and the surrounding medium as destination.

Propagation in stratified media. The *incidence parameter* K for a given wave incident to an interface between two media is defined as the tangential component of the wavevector, that is

$$K = \eta \sin\theta \tag{8}$$

where η is the refractive-index as perceived by the wave travelling in the source medium, and θ is the angle of incidence of a wavevector to an interface. The boundary conditions implied by Maxwell's equations give rise to the crucial observation that K remains constant in the interface between two media [Yariv and Yeh 2003]. Furthermore, as the incident wave U is a plane-wave by assumption, and the top interface as well as all the interfaces between the layers in the stratified slab are parallel by construction, K remains identical for all participating waves in our system for a given θ, the incidence angle of U to the slab. Observe that a direct consequence of this in a y-dependant stratified model is that the wavevectors of all ordinary participating waves at a given layer have identical

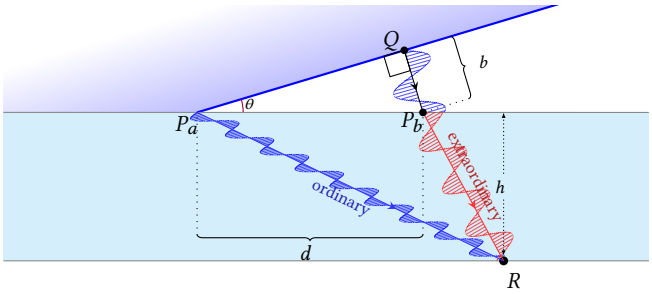

Fig. 3. Illustration of the phase progression of the ordinary and extraordinary waves in the discrete case. A homogeneous optically anisotropic slab of thickness h is portrayed and an incident wavefront (in blue) is refracted into the slab. The horizontal displacement difference between the ordinary and extraordinary waves, d, arises due the difference between the wavevectors' direction, and we are interested in calculating the relative phase shift between the waves induced by the slab. The phase of a wavefront at the exit point R relative to its initial phase at the entry point (P_a for the ordinary wavefront and P_b for the extraordinary) is easily deduced by computing the optical path length travelled by the wave inside the slab. However, due to the offset d between the refraction points the incident plane-wave travels the additional path QP_b before refracting as an e-wave. That distance, denoted b, is then trivially inferred geometrically, viz. $b = d \sin\theta$. The additional optical path length is then dK and the induced phase shift is e^{ikdK}. Note that as K is preserved for all participating waves, the source medium could be either isotropic or anisotropic.

direction, and a similar conclusion follows for the extraordinary waves.

Therefore, the complex amplitudes of a wavefront (originating from either an isotropic or anisotropic source medium) at a point p differs from its complex amplitude at a point $\mathrm{p}' = \mathrm{p} + [\,0,0,d\,]^T$ only by a phase shift that can be trivially deduced geometrically (as illustrated in figure 3). That phase shift depends only on the distance d and the constants k and K, which implies that we can always deduce $\psi\big|_{\mathrm{p}'}$, given knowledge of $\psi\big|_{\mathrm{p}}$.

Following that conclusion, we redefine $\psi(y)$ to be the aggregated Jones vector of the amplitudes of the all participating waves which refract into the slab and reach depth y on the line $\mathrm{p}_a\mathrm{p}_{\mathrm{out}}$. As explained, given $\psi(y_0)$ for some y_0 we can compute $\psi(y_0 - \Delta y)$, that is it holds that

$$\psi(y_0 - \Delta y) = \boldsymbol{\mathcal{P}}_{\Delta y}(y_0)\,\psi(y_0) \tag{9}$$

where $\boldsymbol{\mathcal{P}}_{\Delta y}$ is a linear operator that describes the light propagation through the homogeneous layer and is composed of three operators, the transmission operator $\boldsymbol{\mathcal{T}}_{\Delta y}$, the phase operator $\boldsymbol{\Phi}_{\Delta y}$ and the absorption operator $\boldsymbol{\varsigma}_{\Delta y}$:

$$\boldsymbol{\mathcal{P}}_{\Delta y}(y_0) = \boldsymbol{\mathcal{T}}_{\Delta y}(y_0) \cdot \boldsymbol{\Phi}_{\Delta y}(y_0) \cdot \boldsymbol{\varsigma}_{\Delta y}(y_0) \tag{10}$$

Transmission operator. The transmission operator describes the amplitude ratios of the ordinary and extraordinary waves refracting from $y \equiv y_0$ to the next layer at $y \equiv y_0 - \Delta y$ as well as the cross (ordinary to extraordinary and vice versa) energy transfer:

$$\boldsymbol{\mathcal{T}}(y_0, \Delta y) = \begin{bmatrix} t_{oo} & t_{eo} \\ t_{oe} & t_{ee} \end{bmatrix}\Bigg|_{y_0}^{y_0-\Delta y} \tag{11}$$

The Fresnel transmission coefficients are derived by utilizing the boundary conditions implied by Maxwell's equations [Lekner 1991]. If we ignore the back-reflected energy, those coefficients can be simplified significantly (see appendix E).

Absorption operator. The absorption operator $\boldsymbol{\varsigma}$ expresses the portion of energy absorbed by the medium as an electromagnetic wave travels through it. The absorption happens in accordance to the *Beer-Lambert law* with the extinction coefficients

$$\begin{aligned} \kappa_o &= \mathrm{Im}\{\eta_o\} = \mathrm{Im}\left\{\sqrt{\hat{\epsilon}_o}\right\} \\ \kappa_{\mathrm{ef}}(y) &= \mathrm{Im}\{\eta_{\mathrm{ef}}(y)\} = \mathrm{Im}\left\{\sqrt{\hat{\epsilon}_{\mathrm{ef}}(y)}\right\} \end{aligned} \tag{12}$$

where $\mathrm{Im}\{\cdot\}$ denotes the imaginary part. In addition to the extinction coefficients, the normalized distance a wavefront travels is also required:

$$v_{o,e}(y_0) = \left|\left[\vec{\mathrm{s}}_{o,e}(y_0)\right]_y\right|^{-1} \tag{13}$$

The geometric path length of travel in a layer is then $v_{o,e}(y_0) \cdot \Delta y$ for the ordinary and extraordinary wavefronts, and the absorption operator becomes

$$\boldsymbol{\varsigma}(y_0, \Delta y) = \begin{bmatrix} e^{-\frac{1}{2} v_o \Delta y \cdot \kappa_o} & \\ & e^{-\frac{1}{2} v_e \Delta y \cdot \kappa_{\mathrm{ef}}} \end{bmatrix}\Bigg|_{y_0} \tag{14}$$

Clearly for non-conductive media, i.e. when $\sigma_o, \sigma_e \equiv 0$, it holds that $\eta_o, \eta_e \in \mathbb{R}$ and therefore $\boldsymbol{\varsigma} \equiv \mathrm{I}$. The square root ($\frac{1}{2}$ in the exponents in eq. 14) is taken as we deal with amplitude fields, and not the intensities directly.

Phase progression operator. Finally, the phase operator $\boldsymbol{\Phi}$ serves to advance the phases of the wavefronts as they propagate in the layer by accounting for the *optical distance* (the geometric travel distance $v\Delta y$ multiplied by the refractive-index) of the ordinary and extraordinary wavefronts both inside the slab as well as in the surrounding medium before refraction into the slab. Due to $\psi(y)$ residing on the line $\mathrm{p}_a\mathrm{p}_{\mathrm{out}}$ only the extraordinary wavefront gives rise to additional optical distance outside the slab, which can be computed geometrically in an identical fashion (see figure 3). The phase operator then becomes

$$\boldsymbol{\Phi}(y_0, \Delta y) = \begin{bmatrix} e^{ik\Delta y \cdot \phi_o} & \\ & e^{ik\Delta y \cdot (\phi_e + \Delta\phi_e)} \end{bmatrix}\Bigg|_{y_0} \tag{15}$$

where the phases are

$$\phi_o = v_o \cdot \eta_o \qquad \phi_e(y_0) = v_e(y_0) \cdot \eta_{\mathrm{ef}}(y_0) \tag{16}$$

k is the wavenumber and the induced phase shift of the extraordinary wavefront is

$$\Delta\phi_e(y_0) = \left[(\vec{\mathrm{s}}_e)_z\, v_e - (\vec{\mathrm{s}}_o)_z\, v_o\right]\Big|_{y_0} \cdot K \tag{17}$$

Interference. As wavefronts keep splitting into new ordinary and extraordinary wavefronts at each interface between the homogeneous layers, wave interference occurs—either constructively by waves with similar phases or destructively by those with opposing phases. In practice wave interference for coherent light is computed by summing up the complex amplitudes of superposed waves (by the *principle of superposition of waves* [Born and Wolf 1999]). This

implies that wave interference is a linear operator and commutes with the summation of amplitudes in the aggregated Jones vector $\psi(y)$. Therefore, aggregating the amplitudes of the participating waves at each layer produces correct interference, even if the actual interference occurs at a different, spatial or temporal, point in the process.

3.3 Extending to a differential problem

In this subsection we look at the problem under the limit $\Delta y \to 0$, in which case the discrete homogeneous slabs no longer exist but instead we are looking at a medium with continuously varying optical properties. Under this context we reformulate the problem as an ordinary differential equation (ODE) to which we can then apply analytic and semi-analytic methods to obtain an analytic approximation.

Differential equation derivation. We first begin with a couple of assumptions to ensure correctness:

- Back-reflections, inside the bulk of the medium, are assumed to be negligible. As mentioned, this simplifies the Fresnel transmission coefficients greatly and allows us to only take into account the downwards energy propagation.
- The incidence angle, θ, is restricted such that total-reflection does not occur at any point along that slab, see appendix D for the analytic constraints implied on K in this case.

The first assumption essentially implies that the optical properties of the slab do not change rapidly.

As total-reflection never occurs (by assumption), the operator-valued function that maps $y \mapsto \boldsymbol{\mathcal{P}}$ is analytic in D as a product of analytic functions parameterized by y, and clearly $\lim_{\Delta y\to 0}\boldsymbol{\mathcal{P}} = \mathrm{I}$, therefore ψ is continuous as a function of y. By using the definition of the derivative and applying L'Hôpital's rule we can write

$$\begin{aligned}\frac{\mathrm{d}}{\mathrm{d}y}\psi(y) &= \lim_{\Delta y\to 0}\frac{\psi(y+\Delta y)-\psi(y)}{\Delta y} = \\ &= \left(\lim_{\Delta y\to 0}\frac{\boldsymbol{\mathcal{P}}_{\Delta y}(y)-\mathrm{I}}{\Delta y}\right)\psi(y) = \\ &= \left(\lim_{\Delta y\to 0}\frac{\mathrm{d}}{\mathrm{d}(\Delta y)}\boldsymbol{\mathcal{P}}_{\Delta y}(y)\right)\psi(y) = \boldsymbol{\mathcal{A}}(y)\psi(y)\end{aligned} \tag{18}$$

which, together with the boundary conditions at the upper interface, describes an homogeneous ordinary operator-valued differential equation:

$$\begin{aligned}\frac{\mathrm{d}}{\mathrm{d}y}\psi(y) &= \boldsymbol{\mathcal{A}}(y)\psi(y) \\ \psi(0) &= \mathrm{T}_{\mathrm{in}}\hat{\psi}\Big|_{\mathrm{p}_a}\end{aligned} \tag{19}$$

We define the dot diacritic as a shorthand for $\dot{x} = \lim_{\Delta y\to 0}\frac{\mathrm{d}}{\mathrm{d}(\Delta y)}x$, then the linear operator $\boldsymbol{\mathcal{A}}$ becomes (directly by differentiating eq. 10 and taking the limit):

$$\begin{aligned}\boldsymbol{\mathcal{A}}(y) &= \lim_{\Delta y\to 0}\frac{\mathrm{d}}{\mathrm{d}(\Delta y)}\boldsymbol{\mathcal{P}}_{\Delta y}(y) = \\ &= \begin{bmatrix}\dot{t}_{oo}-\frac{1}{2}\nu_o\kappa_o & \dot{t}_{eo}\\ \dot{t}_{oe} & \dot{t}_{ee}-\frac{1}{2}\nu_e\kappa_{\mathrm{ef}}\end{bmatrix} + ik\begin{bmatrix}\phi_o & \\ & \phi_e+\Delta\phi_e\end{bmatrix}\end{aligned} \tag{20}$$

with the explicit formulas for the $\dot{t}_{\xi\zeta}$ coefficients provided in appendix E.

Equations 19, 20 epitomize our light transport problem, we now turn our attention to constructing an analytic approximative expression for the differential equation.

At the homogeneous limit. To see that our derivation makes sense we briefly verify the solution at the homogeneous limit, that is where the optical properties do not vary across the material. Then, $\boldsymbol{\mathcal{A}}$ and $\vec{\mathrm{s}}_{o,e}$ are now independent of y. Furthermore, as under homogeneity $\boldsymbol{\mathcal{T}} \equiv \mathrm{I}$ and thus $\frac{\mathrm{d}}{\mathrm{d}\Delta y}\boldsymbol{\mathcal{T}} \equiv 0$, it holds that $\boldsymbol{\mathcal{A}}$ is diagonal. Therefore, as the operator $\boldsymbol{\mathcal{A}}$ commutes now with itself the solution to the ODE (equation 19) is simply:

$$\begin{aligned}e^{\int_0^\tau \mathrm{d}y\boldsymbol{\mathcal{A}}} &= e^{\tau\boldsymbol{\mathcal{A}}} = \\ &= \begin{bmatrix}e^{-\frac{1}{2}(\tau\nu_o)\kappa_o} & \\ & e^{-\frac{1}{2}(\tau\nu_e)\kappa_{\mathrm{ef}}}\end{bmatrix}\begin{bmatrix}e^{ik\tau\phi_o} & \\ & e^{ik\tau(\phi_e+\Delta\phi_e)}\end{bmatrix}\end{aligned} \tag{21}$$

The values $\tau\nu_{o,e}$ are now the linear distances travelled by the ordinary and extraordinary waves throughout the entire material, therefore the first matrix is simply the absorption by the material. Similarly, $\tau\phi_{o,e}$ become the phase progression due to optical path distance inside the material and $\tau\Delta\phi_e$ is the relative phase shift.

Equation 21 agrees with the formulation derived by Steinberg [2019] (ignoring internal reflections) for the homogeneous case.

4 ANALYTIC SOLUTION TO THE LIGHT TRANSPORT ODE

Given the differential equation 19, we denote the solution as e^{Ω}. That is e^{Ω} is the complex 2×2 matrix that satisfies

$$\psi(y) = e^{\Omega(y)}\psi(0) \tag{22}$$

We proceed by rewriting the operator $\boldsymbol{\mathcal{A}}$ as a sum of products of scalar functions with constant matrices

$$\boldsymbol{\mathcal{A}}(y) = a(y)\,\mathrm{I} + \sum_{j=1}^{3} b_j(y)\,\mathrm{X}_j \tag{23}$$

where the decomposition is under the following basis

$$\mathrm{X}_1 = \begin{bmatrix}0 & 1\\ 0 & 0\end{bmatrix} \qquad \mathrm{X}_2 = \begin{bmatrix}0 & 0\\ 1 & 0\end{bmatrix} \qquad \mathrm{X}_3 = \begin{bmatrix}1 & 0\\ 0 & -1\end{bmatrix} \tag{24}$$

(the functions $a, b_{1,2,3}$ are chosen such that the equality holds). Then, the problem of computing e^{Ω} is equivalent to the problem of finding a solution to the following four scalar ordinary differential equations:

$$\frac{\mathrm{d}}{\mathrm{d}y}g_1 = -b_2 g_1^2 + 2b_3 g_1 + b_1 \tag{25}$$

$$\frac{\mathrm{d}}{\mathrm{d}y}g_2 = 2\left(g_1 b_2 - b_3\right)g_2 + b_2 \tag{26}$$

$$\frac{\mathrm{d}}{\mathrm{d}y}g_3 = -b_2 g_1 + b_3 \tag{27}$$

$$\frac{\mathrm{d}}{\mathrm{d}y}f = a \tag{28}$$

with initial conditions $g_1(0) = g_2(0) = g_3(0) = f(0) = 0$. If solutions to f, g_1, g_2 and g_3 were to be found, the final solution would then become

$$e^{\Omega} = e^{f} \begin{bmatrix} (1 + g_1 g_2)\, e^{g_3} & g_1 e^{-g_3} \\ g_2 e^{g_3} & e^{-g_3} \end{bmatrix} \tag{29}$$

Equation 29 serves as the first part of our primary contribution and its derivation is provided in detail in appendix A. Note that this is not an approximation, but an exact analytic expression for the solution. Intuitively, the strength of this representation of the solution lies in the fact that we have factored out a considerable amount of "non-linearity" from the initial operator-valued ODE (equation 19) into the exponents in equation 29. As the functions $f, g_{1,2,3}$ are all complex, those exponents give rise to the highly oscillatory behaviour with varying frequencies that the operator $\boldsymbol{\mathcal{A}}$ exhibits. However this behaviour is mostly eliminated from the scalar functions $f, g_{1,2,3}$, and indeed, while solving the original operator-valued ODE is virtually intractable, the scalar functions are far more amenable to analytic and semi-analytic methods.

In order to demonstrate the vast contrast between the behaviours of $\boldsymbol{\mathcal{A}}$ and the functions $f, g_{1,2,3}$, as an experiment we solved those ODEs directly by quadrature using MATLAB™'s ode45 ODE solver. The runtime of the ODE solver when applied to equation 19 is on the order of tens of hours (depending on input), while the scalar functions are solved in seconds to minutes (on same input). See section 5.3 for runtimes.

Physical meaning of the functions f, g_1, g_2 and g_3. The matrix exponentials representation of the light transport ODE was generated by a purely mathematical approach. Nonetheless, some physical meaning can be extracted from the quantities in the solution e^{Ω} (equation 29).

Note that e^{f} serves to advance the overall complex amplitude of the entire system, while e^{g_3} is essentially the complex amplitude difference between the ordinary and extraordinary components. The imaginary parts of f and g_3, therefore, carry the crucial system phase information.

Finally, notice that when $g_1 \equiv g_2 \equiv 0$ no interference is present. The functions g_1 and g_2 represent then the cross-component amplitude transfer and phase-shift.

4.1 Analytic Representations for f and $g_{1,2,3}$

While the ODE for the functions f, g_1, g_2, g_3 (equations 25-28) are far "better behaved" than the operator $\boldsymbol{\mathcal{A}}$, they still do no admit a general analytic solution in closed-form. We exploit the tractability of those scalar ODEs to analytic methods to first simplify the expressions and then produce a closed-form approximative expression to the functions g_1, g_2 written as a finite sum of Gaussian integrals. As f and g_3 are separable we simply employ a Taylor power series to guarantee a solution to f and g_3 for any analytic functions $a, b_{1,2,3}$. The analytic methods that were employed are explained in detail in appendix B, and in this subsection we list the final results:

$$g_1(y) \approx \sqrt{2\pi} \cdot e^{2g_3(y) - \frac{\alpha^2}{2}} \cdot \cdot \int_0^y \phi(i\alpha + i\beta\xi)\, \mathcal{T}_n \left\{ e^{-2\,\mathrm{Re}\{g_3(\xi)\}} b_1(\xi) \right\} \mathrm{d}\xi \tag{30}$$

$$g_2(y) \approx \sqrt{2\pi} \cdot e^{-2g_3(y) + \frac{\alpha^2}{2}} \cdot \cdot \int_0^y \phi(\alpha + \beta\xi)\, \mathcal{T}_n \left\{ e^{2\,\mathrm{Re}\{g_3(\xi)\}} b_2(\xi) \right\} \mathrm{d}\xi \tag{31}$$

$$g_3(y) \approx \int_0^y \mathcal{T}_n \{ b_3(\xi) \}\, \mathrm{d}\xi \tag{32}$$

$$f(y) \approx \int_0^y \mathcal{T}_n \{ a(\xi) \}\, \mathrm{d}\xi \tag{33}$$

with $\mathrm{Re}\{\cdot\}$ denoting the real part, $\mathcal{T}_n$ being the Taylor expansion operator and the Gaussian function $\phi(x) = \frac{1}{\sqrt{2\pi}} e^{-\frac{x^2}{2}}$. The values $\alpha, \beta \in \mathbb{C}$ are given by

$$\alpha = \frac{(1-i)\, c_1}{\sqrt{2c_2}} \qquad \beta = (1-i)\sqrt{2c_2} \tag{34}$$

where $\mathcal{T}_2 \{ \mathrm{Im}\{g_3(y)\} \} = c_1 y + c_2 y^2$. See appendix B for the meaning of α and β.

To compute g_1 and g_2 (equations 30-31) in closed-form we use the following well-known identities of Gaussian integrals:

$$\int_0^x \phi(\alpha + \beta\xi)\, \xi^n\, \mathrm{d}\xi = \frac{1}{\beta^{n+1}} \sum_{m=0}^{n} \binom{n}{m} (-\alpha)^{n-m} \cdot \cdot \left[\int_0^{\alpha+\beta x} \phi(\xi)\, \xi^m\, \mathrm{d}\xi - \int_0^{\alpha} \phi(\xi)\, \xi^m\, \mathrm{d}\xi \right] \tag{35}$$

$$\int_0^x \phi(\xi)\, \xi^{2n+1}\, \mathrm{d}\xi = -\phi(x) \sum_{k=0}^{n} \frac{2n!_{(2)}}{2k!_{(2)}} x^{2k}$$

$$\int_0^x \phi(\xi)\, \xi^{2n+2}\, \mathrm{d}\xi = -\phi(x) \sum_{k=0}^{n} \frac{(2n+1)!_{(2)}}{(2k+1)!_{(2)}} x^{2k+1} + + (2n+1)!_{(2)} \sqrt{\frac{\pi}{2}}\, \mathrm{erf}\left(\frac{x}{\sqrt{2}} \right) \tag{36}$$

where the $!_{(2)}$ denotes the double-factorial. For completeness we derive those three identities in appendix B as well. The complex-valued error function that appears in equation 36 can not be analytically evaluated in closed-form (using elementary functions), however the related *Faddeeva function* can be computed accurately by a vectorized algorithm [Abrarov and Quine 2011, 2018] suitable for GPU computations.

Note that a singularity arises when $c_2 = 0$, in which case the quadratic approximant for $\mathrm{Im}\{g_3(y)\}$ reduces into a linear function, and the Gaussian integrals become simple exponential integrals.

Equations 30-33, together with equation 29, complete our primary contribution and provide a closed-form analytic expression to the light transport solution e^{Ω} for any optical properties described as analytic functions.

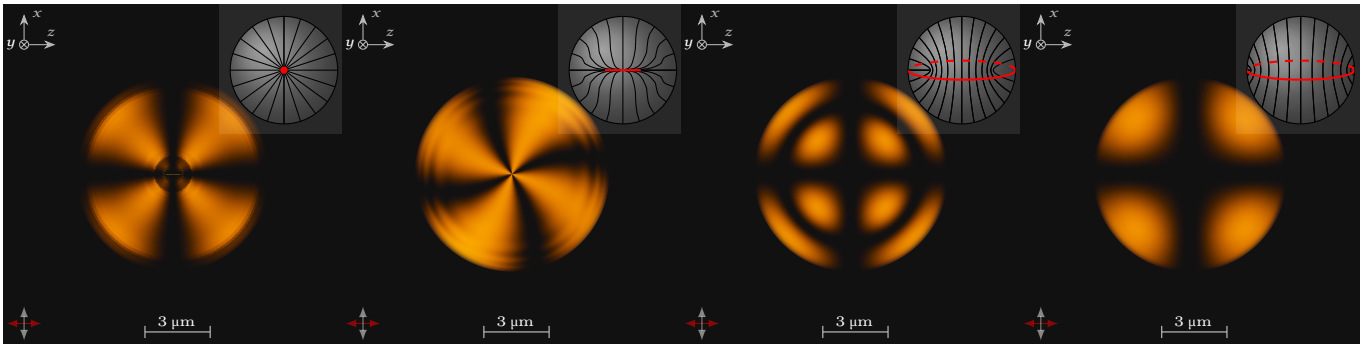

(a) Radial hedgehog defect (b) π-wall defect (c) Disclination ring defect at collapse (d) Ring defect at high voltages

Fig. 4. E12 liquid-crystal microdroplets rendered under cross-polarized light. The droplets are of $9\,\mu\mathrm{m}$ in diameter, illuminated by a $590\,\mathrm{nm}$ light. The configuration of the director field (with defects illustrated in red) as well as the orientation of the polarizers are depicted in the top right and bottom left corners of the figures, respectively. The E12 nematic admits an ordinary refractive-index of 1.52 and an extraordinary refractive-index of 1.74 at room temperature and at $590\,\mathrm{nm}$ radiation. The refractive-index of the surrounding isotropic PDMS (polydimethylsiloxane) is 1.43. Due to the rapid change of the optic axis, especially at the center in the radial configurations (a-b), artefacts arise due to accuracy fall-off of the method. Numeric imprecision errors also arise around the edges. For comparison, micrographs of microdroplets with topologies similar to (b) and (d) can be seen in figure 5. See subsection 5.1 for further discussion.

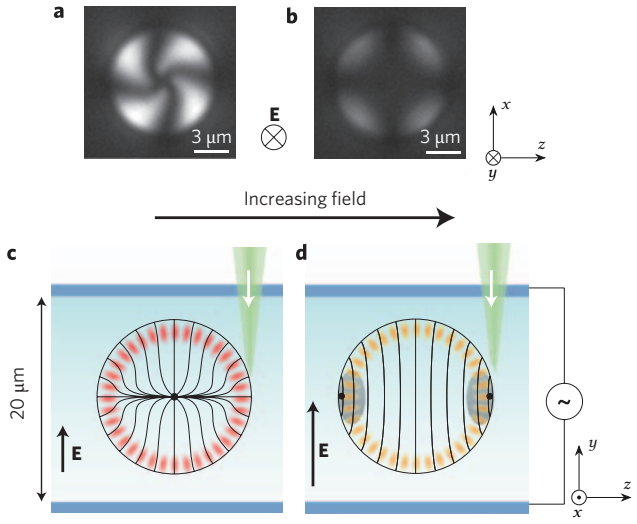

Fig. 5. An E12 liquid-crystal microdroplet with a diameter of $9.30\,\mu\mathrm{m}$ used as a microresonator shows the topological transformation the microdroplet undergoes when an external electric field is applied at increasing intensities. The microdroplet is viewed under polarized microscopy when subject to (a) a $1.90\,V_{\mathrm{RMS}}\,\mu\mathrm{m}^{-1}$ field and (b) a $2.60\,V_{\mathrm{RMS}}\,\mu\mathrm{m}^{-1}$ field. The respective director configurations are shown in (c) as the defect topology changes from a radial hedgehog defect into a π-wall defect in the plane perpendicular to the applied electric field, and in (d) once some threshold voltage is reached the π-wall eventually collapses into an equatorial disclination ring. Reprinted with permission from: Springer Nature, "Electrically tunable liquid crystal optical microresonators" by M. Humar, M. Ravnik, S. Pajk, I. Muševič, ©2009 [Humar et al. 2009].

4.2 Practical Considerations

For the approximant forms of $f, g_{1,2,3}$ (eq. 30, 31, 32, 33) to make sense we need to make an additional assumption: $a, b_{1,2,3}$ are analytic functions, therefore $e^{-2\,\mathrm{Re}\{g_3\}}b_{1,2}$ are also analytic, and the Taylor series of those function converge at some neighbourhood around the expansion point, we then assume that this interval of convergence contains $[0, -\tau]$ and that the truncated series, up to some expansion order n chosen a priori, is reasonably accurate. In practice this assumption holds almost always.

To generalize the solution e^{Ω} (eq. 29) to any incidence angle, slab thickness and wavenumber we first note that the incidence angle θ arises only in the incidence parameter K, which remains constant across all participating wavefronts, therefore K is treated as an unknown constant during integration and is taken as an input during the evaluation of the solution. This allows us to integrate the functions $f, g_{1,2,3}$ during the pre-computation stage per each material only, and efficiently evaluate the solution e^{Ω} at run-time for each incident wavefront of any polarization state, intensity or incidence angle. As the thickness of the slab, τ, is also an input to those functions, it can also be varied at run-time, and the light transport up to any point inside the slab can be easily evaluated.

Quantifying the error. As discussed, the error is dominated by the divergence of the approximations for the solutions of g_1 and g_2 (eq. 30-31). In turn, the accuracy of those functions depends on the accuracy of the quadratic representation of the imaginary part of g_3, viz. $\mathcal{T}_2\{\mathrm{Im}\{g_3\}\}$. We define the function $\mathfrak{e}(y)$ that expresses the count of phase cycles by which the highly oscillatory imaginary exponential term in g_1, g_2 diverges when the phase is represented by the quadratic approximant:

$$\mathfrak{e}(y) = |\mathrm{Im}\{g_3(y) - \mathcal{T}_2\{g_3(y)\}\}| \tag{37}$$

Based on our results, we have chosen the ad hoc value $\frac{\pi}{2}$ such that when $\mathfrak{e}(y) \leq \frac{\pi}{2}$ the solution e^{Ω} is exact for all intents and purposes.

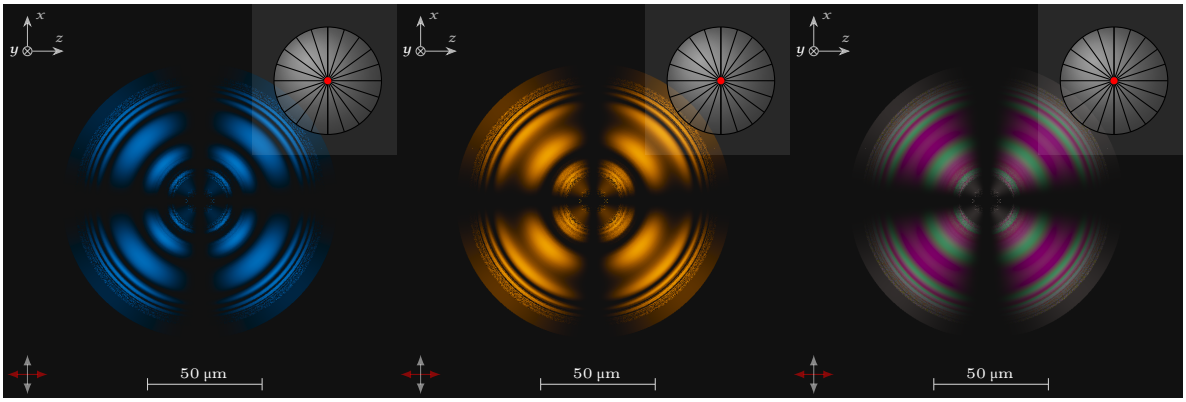

Fig. 6. 122 µm E12 liquid-crystal radial droplets with homeotropic anchoring rendered under cross-polarized light of (left to right) 480 nm, 585 nm and white light (illuminant E). The configuration of the director field (with defects illustrated in red) as well as the orientation of the polarizers are depicted in the top right and bottom left corners of the figures, respectively. The optical configurations of the nematic and the isotropic surrounding medium are identical to figure 4. The artefacts at the center are the same rendering errors that arise with smaller microdroplets as well due to the point defect at the center of the droplet. The noise at the edges is spatial aliasing due to under-sampling. See subsection 5.1 for further discussion.

In practice, the solution renders accurate images for far greater y values. This is mainly due to the fact that g_1, g_2 retain an accurate oscillatory shape for a significant interval after the functions diverge from the ground truth (see figure 13). The frequency of oscillation carries a far greater significance for the reproduction of fringe patterns than the peak amplitudes.

Implementation details. The solution to the light transport equation, e^{Ω}, is in practice simply an analytic form for the coherent bidirectional transmittance distribution function (BTDF) of the material, and can be easily integrated into any spectral renderer. Rendering of optically anisotropic materials with our rendering framework is thus a two-stage process, which we implemented as follows:

(1) Offline integration. First, given a material's optical properties (provided as arbitrary symbolic functions) we start with generating analytic expressions for the functions $f, g_{1,2,3}$ by symbolically integrating equations 30-33 using the MATLAB™ API. The computed analytic expressions are then consumed by the GNU Compiler Collection (gcc) and the optimized intermediate GIMPLE representations are written out as GLSL routines.
(2) Rendering. Those generated artefacts are simply the analytic representations of $f, g_{1,2,3}$ that take as input the wavelength, incidence angle and material thickness (in the form of the wavenumber k, incident parameter K and the distance τ) for which the light transport equation is to be evaluated. Those functions give rise to the solution e^{Ω} (equation 29), i.e. the BTDF, and require no specialized frameworks, like ODE solvers, to be evaluated. Thus integration into any spectral renderer is trivial.

Additional user-supplied variables can be defined as well, which will also be taken as input arguments and evaluated at runtime. Those variables can, e.g., vary the optical properties spatially across the surface, a simple technique that has been used for our demonstrated results.

See our supplemental material, where we include a sample implementation that renders the light transport through inhomogeneous optically anisotropic materials with user-supplied optical properties and a light source of any wavelength and polarization.

5 RESULTS

5.1 Liquid-Crystal Droplets and Shells

Liquid-crystal droplets. "Interesting things happen when liquid crystals are confined to small cavities" [NEM 1995]. Liquid-crystals constitute a class of soft condensed matter that possess fascinating unique properties, granting them a great deal of practical applications. The molecular internal structure of liquid-crystals is typically of long rod-shaped molecules, inducing significant macroscopic anisotropic properties. The direction of the preferred orientation of those molecules—the direction of the optic axis—is described by the *nematic director field*. The director field arranges itself such that the elastic free energy of the liquid-crystal is minimized, and depends on the topological shape of the liquid-crystal, the anchoring at the boundary as well as other forces at play. When liquid-crystals are suspended in liquid, spherical droplets form which usually give rise to topological defects in their structure. Those defects stabilize or destabilize the structure of the director field, potentially limiting its ability to transform its topological configuration, e.g., when an external electric field is applied. See de Gennes and Prost [1993] for a comprehensive review on liquid-crystals.

At rest, with a homeotropic surface anchoring, a liquid-crystal droplet takes the form of a radial hedgehog, with its entire director field pointing directly outwards and a point defect arises at the center (see figure 4a). The point defect can not be annihilated [Stark 2001], however it can morph into other defects [Kanke and Sasaki 2013]. When an external electric field is applied such a transformation occurs and the droplet undergoes significant topological

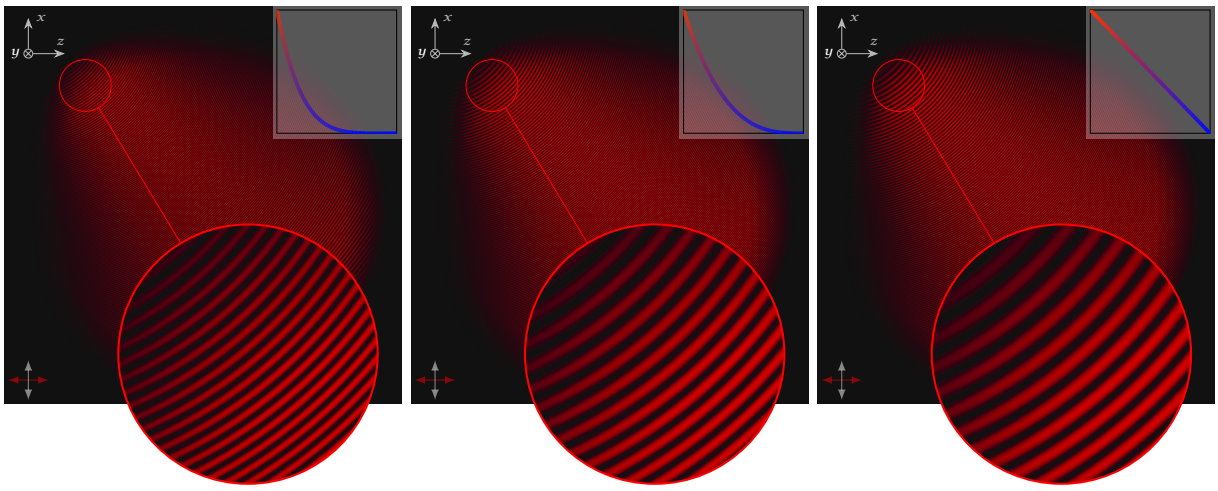

Fig. 7. Fringe patterns that arise as a result of interference as light refracts through a E44 liquid-crystal plate of thickness $\tau = 0.80\,\mathrm{mm}$. Viewed under cross-polarizers and $640\,\mathrm{nm}$ light. One side of the plate was heated to $368\,\mathrm{K}$ while the other remains at $278\,\mathrm{K}$, causing a temperature gradient that gives rise to non-uniform changes in the liquid-crystal's refractive-indices. As a result, the distance between the fringes depends on the heat diffusion. The extraordinary refractive-index of the E44 is modulated from 1.8235 ($T = 278\,\mathrm{K}$) to 1.7035 ($T = 368\,\mathrm{K}$), while the ordinary refractive-index remains fixed at 1.53. The state of the heat diffusion process is illustrated in the upper right corner as a plot: The x-axis corresponds to depth in the plate while the y-axis is temperature. The figures are in chronological order from left to right, such that the figure on the left happens just after the process begins and the figure on the right is once equilibrium is reached. Note that while the heat distribution and incident energy are azimuthally symmetric, the director field is not and therefore the pattern is not radial. The director field is constant and set to about $-\frac{1}{2\sqrt{2}}\vec{\mathrm{x}} + \frac{1}{2\sqrt{2}}\vec{\mathrm{y}} + \frac{\sqrt{3}}{2}\vec{\mathrm{z}}$. See figure 8 and subsection 5.2 for an overview of the experiment.

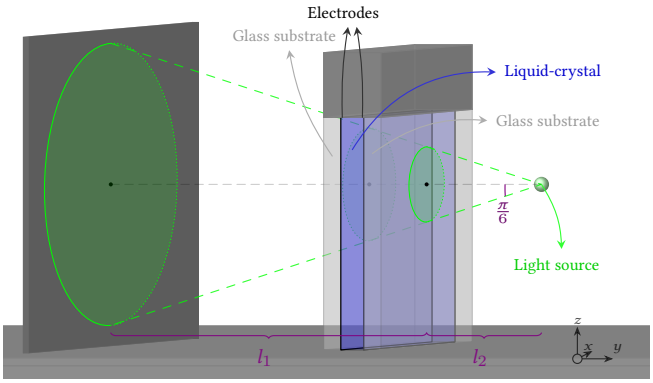

Fig. 8. Illustration of an experiment involving liquid-crystal (in blue) suspended in-between two flat glass plates (bright gray). Transparent, thin layers of indium-oxide (black), which are evaporated onto the glass substrates and act as electrodes in order to control the liquid-crystal's director field. A light source (green) emits a cone-shaped beam that passes through the liquid-crystal plate and gives rise to an interference pattern that is visible on the screen (left). When one of the glass plates is heated, as described in subsection 5.2, the liquid-crystal plate experiences heat diffusion and the state of the diffusion process can be estimated by measuring the distance between the fringes in the resulting pattern (see figure 7).

changes, which depend on its degree-of-birefringence, $\Delta\eta$. The radial hedgehog, when $\Delta\eta$ is positive, first transforms into a π-wall defect in the plane perpendicular to the electric field; and at some threshold voltage the defect finally breaks up and is expelled into the surface resulting in a equatorial defect ring [Bodnar et al. 1991; Lopez-Leon and Fernandez-Nieves 2011] (see figure 5). This process was rendered using our method and can be seen in figure 4. As liquid-crystal are a media where the optic properties can change rapidly, especially around the defects, it is difficult to achieve a precise analytic expression for the light transport. The radial microdroplet (figure 4a) was rendered with the light transport solution, e^{Ω}, evaluated 2 to 4 times throughout the droplet for better accuracy, nonetheless clear errors arise around the defect at the center of the droplet. The π-wall defect (figure 4b) is notoriously hard to render as the director field adopts a complex topology in the interior regions of the droplet, this causes very large and very small numbers to arise in the integrated analytic expression for the functions $f, g_{1,2,3}$, which causes significant numeric imprecisions when evaluated on the GPU. Nonetheless, the patterns are reproduced faithfully and agree with Humar et al. [2009]; Prishchepa et al. [2008].

To help identify the topology, we visualize the orientation of the director field using small insets in the top right corners of figures 4 and 6. The insets depict the droplet when viewed from the side (looking in direction $-x$) such that they are illuminated from the bottom and the camera is located on top (same orientation as in figures 5c, 5d). The black lines illustrate the direction of the director field, i.e. the direction of the optic axis, inside the droplet while the red lines illustrate the position and topology of the defect.

In order for our rendering method to apply to droplets we need to approximate the incident surface with a flat surface, as discussed previously. As the divergence between the ordinary and extraordinary wavevectors is small, this is not an issue even with highly

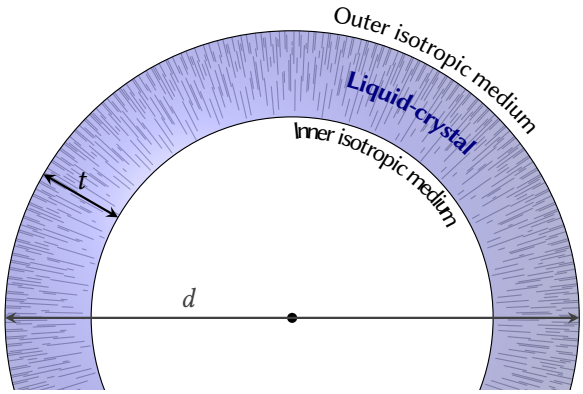

Fig. 9. Geometry of a liquid-crystal shell (in blue) of diameter d and wall thickness t under homeotropic anchoring. The inner and outer isotropic solutions are considered to be identical.

birefringent liquid-crystals like 5CB. The geometry of the surface at the exit point is of no consequence as the entire light transport concentrates at a single point on exit. Applying those principles allows us to extend our method to almost arbitrary smooth surfaces.

Larger droplets and shells. We have also rendered larger droplets, seen in figure 6, with different light wavelengths. At the edges of those droplets the frequency of the fringe rings greatly exceeds the sampling frequency and spatial aliasing arises. Those are classic under-sampling artefacts, and similar behaviour was observed by Steinberg [2019] when rendering homogeneous anisotropic media.

In addition, liquid-crystal shells comprising of the well studied 5CB (4-Cyano-4'-pentylbiphenyl) liquid-crystal with isotropic interiors were rendered (see figure 1) using the presented method and the patterns agree very well with similar shells that were observed under polarized microscopy by Geng et al. [2016]. The shells are $200\,\mu\text{m}$ in diameter with a wall thickness of $13\,\mu\text{m}$ and admit homeotropic anchoring of the director field at the surface (i.e., the director field is pointing inwards at the surface), see figure 9 for an illustration of the geometry of the liquid-crystal shell. The ordinary and extraordinary refractive-indices of the nematic phase of 5CB are 1.5340 and 1.7070, respectively, at room temperature and $590\,\text{nm}$ light [Tkachenko et al. 2006]. The surrounding medium, as well as the isotropic mixture inside the shells, is assumed to be a glycerol-water mixture, which admits a refractive-index of about 1.42 at a wavelength of $590\,\text{nm}$. Note that the fringe patterns of the E12 microdroplets, once the point defect has collapsed into the disclination ring defect (figures 4c, 4d), are akin to the fringe pattern that arise in the center of the shells (figures 1). This is no coincidence, and by comparing the director fields we observe that the birefringence effect in both topologies are very similar: The director field in the interior of the microdroplets generates very little birefringence while both the shells and microdroplets have identical surface anchoring, resulting in similar director fields at the region close to the surface.

5.2 Heated Liquid-Crystal Plate

Measuring thermal gradients in crystals is another potential application and is an area of active research [Kocharyan et al. 2015]. We present a hypothetical experiment where a liquid-crystal plate is subject to non-uniform heat, and show how our method can be applied.

Variations in the director field is the most common source of non-homogeneity in liquid-crystals. However, a scenario where one side of a crystal, or a liquid-crystal, plate is subject to high heat can induce a refractive-indices gradient with respect to the heat diffusion through the plate [Berman et al. 1992]. Our setup is as follows (see figure 8): A slab of thickness τ, with a light source emitting a cone-shaped beam with angle $\frac{\pi}{6}$ that passes through the sample causing interference patterns to form on the screen. The liquid-crystal plate has uniform anchoring across the boundary and the director field is electrically aligned in a single direction. One side of the plate is subject to heat, $368\,\text{K}$, while the other remains at $278\,\text{K}$. We assume the liquid-crystal used is E44, which has a melting point—point of equilibrium between crystalline and liquid states—of $272.15\,\text{K}$ and a clearing temperature, i.e. the temperature at which the liquid-crystal becomes isotropic, of $373.15\,\text{K}$ [Gauza et al. 2004]. The molecular structure of the liquid-crystal gives rise to anisotropy in the thermal conductivity as well as optical anisotropy [Ahlers et al. 1994], however as the director field is uniformly aligned, this can be ignored.

The refractive-indices of liquid-crystals fluctuate with temperature, especially the extraordinary refractive-index [Li et al. 2005]. To create an accurate model of the E44 nematic we curve fit the following linear function to E44's extraordinary refractive-index as a function of temperature

$$\eta_e^{\text{E44}}(T) = 2.1942 - \frac{T}{750} \tag{38}$$

with T in Kelvin, while the ordinary refractive-index is kept fixed at 1.53, approximating data measured by Li et al. [2005]. The extraordinary refractive-index is then modulated through the slab with respect to approximate solutions to the heat equation at various points in time, and the resulting slabs are rendered using our method and shown in figure 7. The state of the thermal diffusion process could then be estimated in a (liquid) crystal plate just by measuring the distance between the isochromatic fringes in the produced patterns. Notice that this technique is contact-free, that is it requires no access to the side walls of the plate, a scenario that complicates thermal imaging.

5.3 Evaluation

Finally, we have also created a hypothetical conductive slab where the optic axis, the conductivity and the extraordinary permittivity all vary simultaneously and independently (see our supplemental material). This material is used for evaluation and shows that we can accurately render inhomogeneous anisotropic media with multiple degrees of freedom. The setup is identical to the one used in subsection 5.2 (see figure 8), and the rendered images can be seen in figure 11. Those images were then compared against a ground-truth that was generated by modelling the inhomogeneous slab as

Material		Evaluation Slab	E12 LC microdroplet (hedgehog)	E44 LC plate
Rendering (time per frame)	Our method	69 ms	48.50 ms	58 ms
	4k discrete layers	≈7700 ms	≈8500 ms (fails to converge)	≈8500 ms (fails to converge)
Program generation	Integration	19 min 51 sec	4 min 13 sec	26 min
	Optimization	31 min 2 sec	64.30 sec	60 min 56 sec
	Instruction count	21.70 kdops	8.70 kdops	16.30 kdops
ode45 solver (time per sample)	Scalar ODEs	7 sec	9 sec	15 min 7 sec
	Operator-valued ODE	6 h 26 min	20 h 37 min	20 h 25 min

Table 1. Runtime performance of our method. We have evaluated three materials: The evaluation slab (figure 11), the E12 liquid-crystal microdroplet with a radial hedgehog topology (figure 4a) and the E44 liquid-crystal plate under heat diffusion (figure 7). The resulting patterns were rendered at a 500×500 resolution on an NVIDIA® GeForce® RTX 2080Ti graphics accelerator and the frame times are listed. The rendering times of the brute-force method, using 4k discrete homogeneous layers (used in figure 11), are shown as well and note that the more complicated materials fail to converge with any layer count due to numerical problems. The program generation was done on an Intel® Core™ i9-9900K CPU and the runtimes of the symbolic integration and the program optimization stages are provided, as well as the double-precision floating point instruction count of the generated programs. Finally, we list the runtimes of MATLAB™'s ode45 ODE solver when solving the full operator-valued ODE (equation 19) in comparison to the system of four scalar ODEs (equations 25-28).

a stack of 4096 homogeneous anisotropic layers. The colour deviations were calculated using the CIE DE2000 metric and are shown in figure 11 as well. Compared with the ground-truth the fringe distances in the generated patterns begin to diverge slightly with thicker slabs, however otherwise the patterns are accurate. A numerical evaluation was also performed by comparing the results of our method with numerically differentiated values obtained via MATLAB™'s ode45 ODE solver (see figure 10), and both evaluations show very good agreement.

For completeness, we also detail the computational costs of the presented method in table 1, where we list render durations and precomputation timings as well as the instruction count of the generated GLSL programs. The program generation is done as described in subsection 4.2. The programs were generated with a Taylor expansion order of 7. Significantly faster results can be obtained with lower expansion orders, at the cost of potentially deteriorated accuracy. However, performance has not been our focus and we did not investigate further nor can our implementation be considered optimal.

6 DISCUSSION AND FUTURE WORK

The mathematical framework intrinsic to our technique is an immediate result of the Magnus expansion. We avoid using the Magnus expansion directly as the nested integrals of nested commutators (eq. 41) become exponentially unyielding to symbolic integration. Instead we look at the representation of the solution as a finite product of matrix exponentials subject to a chosen basis of a Lie algebra. The neighbourhood where the representation applies is only limited by the open set D where the input functions are analytic.

This result—representation of the solution as a product of matrix exponentials—which was proven by us in appendix A, in a fashion transcends our discussion: We have shown that an operator-valued ordinary differential equation, where the operator is any 2×2 complex matrix, always has a unique solution, and the problem of finding that solution is reduced to solving 4 scalar ODEs, which are remarkably more tractable to analytic and semi-analytic method. This conclusion does not depend on the discussion that preceded it, and therefore has nothing to do with liquid-crystals or optical anisotropy, per sē. Furthermore, the difficulties that we encountered when devising analytic expressions for the solutions of those 4 ODEs are characteristic to coherent light transport: Very rapidly oscillating integrands due to the fast phase evolution in the visible spectrum. We are therefore hopeful that our presented method can be used or adapted to other problems, light transport or otherwise, in the realm of computer graphics.

Future applications. As outlined briefly in subsection 1.1, we envision the primary applications of our method to be two-fold:

(1) Generation of synthetic datasets. Development of machine learning approaches to deduce various types of information from liquid-crystal micrographs is an area of active research and a major difficulty is the acquisition of large training data. Our rendering method could be utilized by future research in order to render realistic datasets of micrographs, efficiently and accurately.
(2) Deduction of optical properties from micrographs. If the topology of the sample is known then its optical properties, e.g., the refractive indices, can be deduced experimentally by tuning the optical properties used for rendering until the rendering matches the micrograph. This exact approach was used by us to render the microdroplets and shells in figures 4, 1. Likewise, other data can be extracted, for example consider the experiment described in figure 5. By deducing which deformation of the director field gives rise to the optical response captured by the micrograph, we can infer the strength of the applied electric field (if the chemistry of the microdroplet is known). This process could, in theory, be automated and we leave that for future work as well.

Furthermore, while in this paper we keep our attention focused on liquid-crystals—which provide an interesting and comprehensive example of inhomogeneous optically anisotropic media—our method can also be applied to other materials that exhibit spatially varying optical anisotropy. For example, optical anisotropy can be induced in (otherwise isotropic) translucent dielectrics when subject to mechanical stress, a phenomenon known as photoelasticity. The induced degree-of-birefringence is proportional to the stress magnitude and the optic axis aligns with the direction of stress.

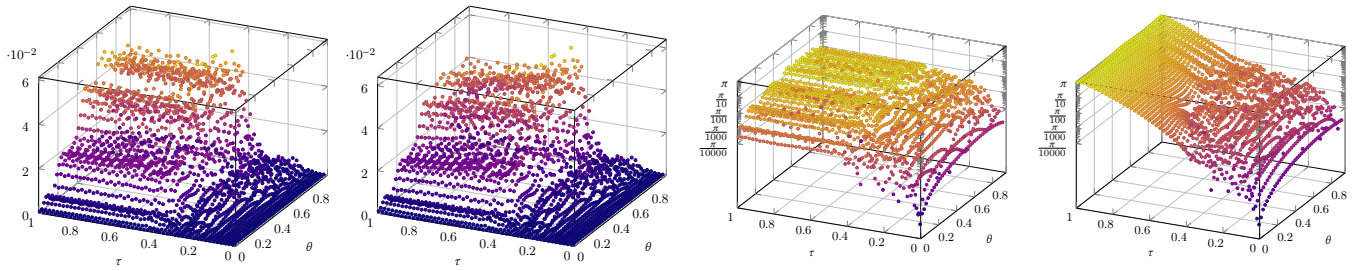

(a) Ordinary amplitude (b) Extraordinary amplitude (c) Ordinary phase (d) Extraordinary phase

Fig. 10. Plots of the errors of (a) the peak amplitude of ordinary wave once refracted though the slab; (b) the peak amplitude of the extraordinary wave; (c) the ordinary wave's phase (logarithmic plot); (d) the extraordinary wave's phase (logarithmic plot). Plotted for a range of values for τ, the slab's thickness and θ, the incident angle, using the evaluation slab. A $500\,\mathrm{nm}$ wavelength light was assumed.

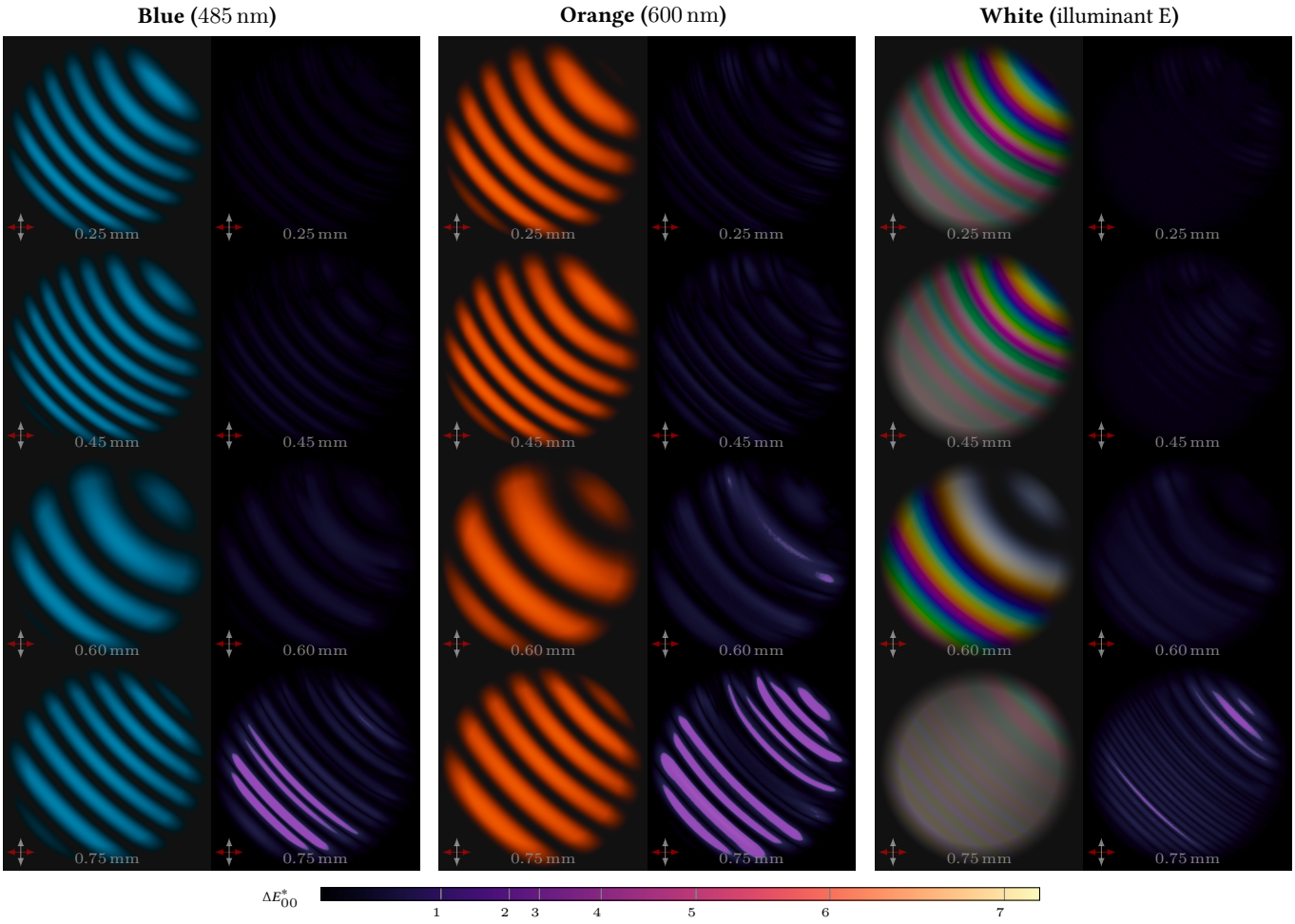

Fig. 11. Interference patterns generated by the evaluation slab (shown on the left in each column) with τ ranging from $0.25\,\mathrm{mm}$ to $0.75\,\mathrm{mm}$, rendered using (left to right) blue light ($485\,\mathrm{nm}$), orange light ($600\,\mathrm{nm}$) and white light (illuminant E). Viewed under cross-polarizers. Those rendered patterns were evaluated against a ground-truth that was modelled and rendered as a stack of 4096 homogenous layers (not shown). The errors between the images rendered using our method and the ground-truth were quantified using the CIE DE2000 formula, and the colour-coded images of ΔE^*_{00}, the CIE DE2000 values, are shown (on the right in each column). As the slab gets thicker the distance between the fringes deviates slightly (<10 %) from the ground-truth, however the patterns are still faithfully reproduced. Minor colour deviations also arise with ΔE^*_{00} values of up to 2 and usually less than 1, indicating very good accuracy.

This has made photoelasticity of great interest in stress analysis, e.g. in masonry, and our method can be used to render the expected isochromatic fringe patterns that arise given a specific stress field.

Optical coherence. We have assumed a fully-coherent monochromatic light ensemble modelled as a plane-wave, however physical light sources are neither truly monochromatic nor infinitely coherent. Optical coherence is the spatial and temporal correlation between the periodic distributions formed by light ensembles and as this correlation diminishes so does the ensemble's ability to be superposed and interfere [Mandel and Wolf 1995]. Spatial coherency of a light source can be described by the *coherence area* ΔA and approximated by an order of magnitude relation: $\Delta A \sim \lambda^2/\Theta$ [Mandel and Wolf 1995], where Θ is the solid angle subtended by the source. See appendix D where a formulation for the maximal possible thickness, τ, as a function of coherence size and incidence angle is provided.

Incoherent energy is commonly aggregated by summing up the intensities (incoherent addition) of the coherent elements, while the loss of coherency is approximated by a coherency kernel (see, e.g., Dong et al. [2015]; Yan et al. [2018]), which is typically a Gaussian matching experimental data [Mashaal et al. 2012]. Those principles could be applied by using a multi-layered structure of inhomogeneous layers and modelling coherency loss between the layers; this approach has been extensively studied (see related work in section 2) and is outside the focus of our work.

Lastly, our assumption of an incident plane-wave allows us to fix the incidence parameter K and facilitates the discussion in section 3. However, it also effectively restricts the scope of our developed formulations to the Fraunhofer region (far-field) only.

Accuracy. The accuracy is generally dominated by the accuracy of the functions g_1 and g_2, which are effectively limited by the divergence of the quadratic approximant for the imaginary part of g_3. Therefore the error is quantifiable by the function $\mathfrak{e}$ (equation 37). This information allows us to understand, at run-time, how accurate the solution is for a given set of input parameters, and if needed, dynamically break up the bulk of the medium into a set of thinner (inhomogeneous) layers and evaluate the coherent light transport at each layer separately. We employed this technique for the rendering of the E12 liquid-crystal microdroplets (figure 4) in order to extend the accuracy of the method to the desired domain.

Scattering. We have ignored scattering and back-reflections inside the bulk of the anisotropic medium as it is beyond the scope of this paper. Nonetheless, this energy can not always be neglected. Simple numeric radiative transport techniques like the "Adding"-method [Prahl 1995] can give rise to a multi-layered framework of inhomogeneous layers, which considers the internal reflections between the layers (e.g., Katsidis and Siapkas [2002]), while non-discrete methods could build upon a combination of our framework and Berreman's 4x4 matrix method [Berreman 1972].

7 CONCLUSION

We have presented a novel rendering technique, formulated under the electromagnetic wave theory, that computes the amplitudes and phases of light propagating through arbitrary inhomogeneous stratified anisotropic media via an analytic approximation to the light transport that accounts for the entire field of amplitudes that arises in the bulk of such media. Our rendering framework is robust, produces physically accurate images at interactive frame-rates, orders of magnitude faster than established research, and provides an analytic error estimate.

REFERENCES

1972. I: Scalar Riccati Differential Equations. In *Riccati Differential Equations*, William T. Reid (Ed.). Mathematics in Science and Engineering, Vol. 86. Elsevier, 1 – 8. https://doi.org/10.1016/S0076-5392(08)61166-2

1995. *Nematic Configurations Within Droplets.* WORLD SCIENTIFIC, 99–181. https://doi.org/10.1142/9789812831910_0003

S.M. Abrarov and B.M. Quine. 2011. Efficient algorithmic implementation of the Voigt/complex error function based on exponential series approximation. *Appl. Math. Comput.* 218, 5 (Nov 2011), 1894–1902. https://doi.org/10.1016/j.amc.2011.06.072

Sanjar M. Abrarov and Brendan M. Quine. 2018. A rational approximation of the Dawson's integral for efficient computation of the complex error function. *Appl. Math. Comput.* 321 (Mar 2018), 526–543. https://doi.org/10.1016/j.amc.2017.10.032

Guenter Ahlers, David S. Cannell, Lars Inge Berge, and Shinichi Sakurai. 1994. Thermal conductivity of the nematic liquid crystal 4-n-pentyl-4'-cyanobiphenyl. *Physical Review E* 49, 1 (Jan 1994), 545–553. https://doi.org/10.1103/physreve.49.545

Alireza Akbarzadeh and Aaron J. Danner. 2010. Generalization of ray tracing in a linear inhomogeneous anisotropic medium: a coordinate-free approach. *J. Opt. Soc. Am. A* 27, 12 (Dec 2010), 2558–2562. https://doi.org/10.1364/JOSAA.27.002558

Marco Ament, Christoph Bergmann, and Daniel Weiskopf. 2014. Refractive Radiative Transfer Equation. *ACM Trans. Graph.* 33, 2, Article 17 (April 2014), 22 pages. https://doi.org/10.1145/2557605

Amir Nader Askarpour, Yang Zhao, and Andrea Alù. 2014. Wave propagation in twisted metamaterials. *Physical Review B* 90, 5 (Aug 2014). https://doi.org/10.1103/physrevb.90.054305

A. L. Aslanyan, L. S. Aslanyan, and Yu. S. Chilingaryan. 2015. On the jones matrix method in a twisted anisotropic medium. *Optics and Spectroscopy* 119, 5 (01 Nov 2015), 869–874. https://doi.org/10.1134/S0030400X15100069

Seung-Hwan Baek, Diego Gutierrez, and Min H. Kim. 2016. Birefractive Stereo Imaging for Single-shot Depth Acquisition. *ACM Trans. Graph.* 35, 6, Article 194 (Nov. 2016), 11 pages. https://doi.org/10.1145/2980179.2980221

Chen Bar, Marina Alterman, Ioannis Gkioulekas, and Anat Levin. 2019. A Monte Carlo framework for rendering speckle statistics in scattering media. *ACM Transactions on Graphics* 38, 4 (Jul 2019), 1–22. https://doi.org/10.1145/3306346.3322950

Viswanath Bavigadda, Emilia Mihaylova, Raghavendra Jallapuram, and Vincent Toal. 2012. Vibration phase mapping using holographic optical element-based electronic speckle pattern interferometry. *Optics and Lasers in Engineering* 50, 8 (Aug 2012), 1161–1167. https://doi.org/10.1016/j.optlaseng.2012.01.020

N. Bennis, I. Merta, A. Kalbarczyk, M. Maciejewski, P. Marc, A. Spadlo, and L.R. Jaroszewicz. 2017. Real time phase modulation measurements in liquid crystals. *Opto-Electronics Review* 25, 2 (Jun 2017), 69–73. https://doi.org/10.1016/j.opelre.2017.03.004

Lonny E. Berman, Michael Hart, and Sushil Sharma. 1992. Adaptive crystal optics for undulator beamlines. *Nuclear Instruments and Methods in Physics Research Section A: Accelerators, Spectrometers, Detectors and Associated Equipment* 321, 3 (Oct 1992), 617–628. https://doi.org/10.1016/0168-9002(92)90074-e

Dwight W. Berreman. 1972. Optics in Stratified and Anisotropic Media: 4×4-Matrix Formulation. *J. Opt. Soc. Am.* 62, 4 (Apr 1972), 502–510. https://doi.org/10.1364/JOSA.62.000502

F. Donald Bloss. 1961. *An introduction to the methods of optical crystallography / F. Donald Bloss.* Saunders College Philadelphia.

Vladimir G. Bodnar, Alexandr V. Koval'chuk, Oleg D. Lavrentovich, V. M. Pergamenshchik, and V. V. Sergan. 1991. <title>Threshold of structural transition in nematic drops with normal boundary conditions in AC electric field</title>. In *Liquid-Crystal Devices and Materials*, Paul S. Drzaic and UziEditors Efron (Eds.). SPIE. https://doi.org/10.1117/12.44699

M. Born and E. Wolf. 1999. *Principles of Optics.* Cambridge University Press. 952 pages.

A. C. Callan-Jones, Robert A. Pelcovits, V. A. Slavin, S. Zhang, D. H. Laidlaw, and G. B. Loriot. 2006. Simulation and visualization of topological defects in nematic liquid crystals. *Phys. Rev. E* 74 (Dec 2006), 061701. Issue 6. https://doi.org/10.1103/PhysRevE.74.061701

Chen Cao, Zhong Ren, Baining Guo, and Kun Zhou. 2010. Interactive Rendering of Non-Constant, Refractive Media Using the Ray Equations of Gradient-Index Optics. *Computer Graphics Forum* 29, 4 (Aug 2010), 1375–1382. https://doi.org/10.1111/j.1467-8659.2010.01733.x

Yankai Cao, Huaizhe Yu, Nicholas L. Abbott, and Victor M. Zavala. 2018. Machine Learning Algorithms for Liquid Crystal-Based Sensors. *ACS Sensors* 3, 11 (2018), 2237–2245. https://doi.org/10.1021/acssensors.8b00100 PMID: 30289249.

Charly Collin, Sumanta Pattanaik, Patrick LiKamWa, and Kadi Bouatouch. 2014. Computation of Polarized Subsurface BRDF for Rendering. In *Proceedings of Graphics Interface 2014 (GI '14)*. 201–208.

Tom Cuypers, Tom Haber, Philippe Bekaert, Se Baek Oh, and Ramesh Raskar. 2012. Reflectance model for diffraction. *ACM Transactions on Graphics* 31, 5 (Aug 2012), 1–11. https://doi.org/10.1145/2231816.2231820

E. Ledezma-Sillas D. Tentori, C. Ayala-Díaz. 2008. Matrix model for a twisted medium: liquid crystal cell. https://doi.org/10.1117/12.795282

P.G. de Gennes and J. Prost. 1993. *The Physics of Liquid Crystals*. Clarendon Press. https://books.google.com/books?id=0Nw-dzWz5agC

Arnout De Meyere. 1994. Light propagation and color variations in liquid-crystal displays. *Journal of the Optical Society of America A* 11, 2 (Feb 1994), 731. https://doi.org/10.1364/josaa.11.000731

Hideo Doi, Kazuaki Z. Takahashi, Kenji Tagashira, Jun-ichi Fukuda, and Takeshi Aoyagi. 2019. Machine learning-aided analysis for complex local structure of liquid crystal polymers. *Scientific Reports* 9, 1 (Nov 2019). https://doi.org/10.1038/s41598-019-51238-1

Zhao Dong, Bruce Walter, Steve Marschner, and Donald P. Greenberg. 2015. Predicting Appearance from Measured Microgeometry of Metal Surfaces. *ACM Trans. Graph.* 35, 1 (2015), 9:1–9:13.

K. Eidner, G. Mayer, M. Schmidt, and H. Schmiedel. 1989. Optics in Stratified Media—The Use of Optical Eigenmodes of Uniaxial Crystals in the 4 × 4-Matrix Formalism. *Molecular Crystals and Liquid Crystals Incorporating Nonlinear Optics* 172, 1 (1989), 191–200. https://doi.org/10.1080/00268948908042161

M. Gantri. 2014. Solution of Radiative Transfer Equation with a Continuous and Stochastic Varying Refractive Index by Legendre Transform Method. *Computational and Mathematical Methods in Medicine* 2014 (2014), 1–7. https://doi.org/10.1155/2014/814929

S. Gauza, C. H. Wen, B. Tan, Y. H. Wu, Y. H. Lin, and S. T. Wu. 2004. 46.1: UV-Stable High-Birefringence Low-Viscosity Isothiocyaniane Liquid Crystals and Application to 50-μsec Response Switching Device. *SID Symposium Digest of Technical Papers* 35, 1 (2004), 1304. https://doi.org/10.1889/1.1825755

Yong Geng, JungHyun Noh, and Jan P. F. Lagerwall. 2016. Transmission polarized optical microscopy of short-pitch cholesteric liquid crystal shells. In *Emerging Liquid Crystal Technologies XI*, Liang-Chy Chien, Dick J. Broer, Hirotsugu Kikuchi, and Nelson V.Editors Tabiryan (Eds.). SPIE. https://doi.org/10.1117/12.2216132

Thomas A. Germer, Katelynn A. Sharma, Thomas G. Brown, and James B. Oliver. 2017. Polarized optical scattering by inhomogeneities and surface roughness in an anisotropic thin film. *J. Opt. Soc. Am. A* 34, 11 (Nov 2017), 1974–1984. https://doi.org/10.1364/JOSAA.34.001974

A. Guerreiro, J. C. Costa, M. Gomes, R. A. Alves, and N. A. Silva. 2017. Physical ray-tracing method for anisotropic optical media in GPGPU. https://doi.org/10.1117/12.2272144

Yubing Guo, Miao Jiang, Chenhui Peng, Kai Sun, Oleg Yaroshchuk, Oleg Lavrentovich, and Qi-Huo Wei. 2016. High-Resolution and High-Throughput Plasmonic Photopatterning of Complex Molecular Orientations in Liquid Crystals. *Advanced Materials* 28, 12 (Jan 2016), 2353–2358. https://doi.org/10.1002/adma.201506002

Diego Gutierrez, Adolfo Munoz, Oscar Anson, and Francisco J. Seron. 2008. Non-linear volume photon mapping. In *ACM SIGGRAPH ASIA 2008 courses on - SIGGRAPH Asia '08*. ACM Press. https://doi.org/10.1145/1508044.1508109

Ji-Huan He. 1999. Homotopy perturbation technique. *Computer Methods in Applied Mechanics and Engineering* 178, 3–4 (Aug 1999), 257–262. https://doi.org/10.1016/s0045-7825(99)00018-3

M. Humar, M. Ravnik, S. Pajk, and I. Muševič. 2009. Electrically tunable liquid crystal optical microresonators. *Nature Photonics* 3, 10 (Sep 2009), 595–600. https://doi.org/10.1038/nphoton.2009.170

Wenzel Jakob, Eugene D'Eon, Otto Jakob, and Steve Marschner. 2014. A Comprehensive Framework for Rendering Layered Materials. *ACM Transactions on Graphics (Proceedings of SIGGRAPH)* 33, 4 (July 2014), 118:1–118:14. https://doi.org/10.1145/2601097.2601139

Adrian Jarabo and Victor Arellano. 2018. Bidirectional Rendering of Vector Light Transport. *Computer Graphics Forum* 37, 6 (2018), 96–105. https://doi.org/10.1111/cgf.13314

Masaki Kanke and Kazuo Sasaki. 2013. Equilibrium Configuration in a Nematic Liquid Crystal Droplet with Homeotropic Anchoring of Finite Strength. *Journal of the Physical Society of Japan* 82, 9 (Sep 2013), 94605. https://doi.org/10.7566/jpsj.82.094605

Charalambos C. Katsidis and Dimitrios I. Siapkas. 2002. General transfer-matrix method for optical multilayer systems with coherent, partially coherent, and incoherent interference. *Appl. Opt.* 41, 19 (Jul 2002), 3978–3987. https://doi.org/10.1364/AO.41.003978

S. Kaur, Y.-J. Kim, H. Milton, D. Mistry, I. M. Syed, J. Bailey, K. S. Novoselov, J. C. Jones, P. B. Morgan, J. Clamp, and et al. 2016. Graphene electrodes for adaptive liquid crystal contact lenses. *Optics Express* 24, 8 (Apr 2016), 8782. https://doi.org/10.1364/oe.24.008782

Yasaman Kiasat, Zsolt Szabo, Xudong Chen, and Erping Li. 2014. Light interaction with multilayer arbitrary anisotropic structure: an explicit analytical solution and application for subwavelength imaging. *J. Opt. Soc. Am. B* 31, 3 (Mar 2014), 648–655. https://doi.org/10.1364/JOSAB.31.000648

Mingyun Kim, Kyun Joo Park, Seunghwan Seok, Jong Min Ok, Hee-Tae Jung, Jaehoon Choe, and Do Hyun Kim. 2015. Fabrication of Microcapsules for Dye-Doped Polymer-Dispersed Liquid Crystal-Based Smart Windows. *ACS Applied Materials & Interfaces* 7, 32 (Aug 2015), 17904–17909. https://doi.org/10.1021/acsami.5b04496

V. R. Kocharyan, A. S. Gogolev, A. E. Movsisyan, A. H. Beybutyan, S. G. Khlopuzyan, and L. R. Aloyan. 2015. X-ray diffraction method for determination of interplanar spacing and temperature distribution in crystals under an external temperature gradient. *Journal of Applied Crystallography* 48, 3 (May 2015), 853–856. https://doi.org/10.1107/s1600576715006913

I.S. Kolomiets. 2013. Studying anisotropic properties of longitudinal inhomogeneous nondepolarizing media with elliptical phase anisotropy. *Semiconductor Physics Quantum Electronics and Optoelectronics* 16, 4 (Dec 2013), 366–373. https://doi.org/10.15407/spqeo16.04.366

Yu. A. Kravtsov, B. Bieg, and K. Yu. Bliokh. 2007. Stokes-vector evolution in a weakly anisotropic inhomogeneous medium. *Journal of the Optical Society of America A* 24, 10 (Sep 2007), 3388. https://doi.org/10.1364/josaa.24.003388

Pedro Latorre, Francisco J. Seron, and Diego Gutierrez. 2012. Birefringence: calculation of refracted ray paths in biaxial crystals. *The Visual Computer* 28, 4 (01 Apr 2012), 341–356. https://doi.org/10.1007/s00371-011-0619-2

Mon-Juan Lee, Chi-Hao Lin, and Wei Lee. 2015. Liquid-crystal-based biosensing beyond texture observations. In *Liquid Crystals XIX*, Iam ChoonEditor Khoo (Ed.). SPIE. https://doi.org/10.1117/12.2187818

J. Lekner. 1991. Reflection and refraction by uniaxial crystals. *Journal of Physics Condensed Matter* 3 (Aug. 1991), 6121–6133. https://doi.org/10.1088/0953-8984/3/32/017

Anat Levin, Daniel Glasner, Ying Xiong, Fredo Durand, Bill Freeman, Wojciech Matusik, and Todd Zickler. 2013. Fabricating BRDFs at High Spatial Resolution Using Wave Optics. *ACM Transaction of Graphics* (2013).

J. Li, C.-H. Wen, S. Gauza, R. Lu, and S.-T. Wu. 2005. Refractive Indices of Liquid Crystals for Display Applications. *Journal of Display Technology* 1, 1 (Sep 2005), 51–61. https://doi.org/10.1109/jdt.2005.853357

Teresa Lopez-Leon and Alberto Fernandez-Nieves. 2011. Drops and shells of liquid crystal. *Colloid and Polymer Science* 289, 4 (Jan 2011), 345–359. https://doi.org/10.1007/s00396-010-2367-7

Jens G. Magnus and Stefan Bruckner. 2018. Interactive Dynamic Volume Illumination with Refraction and Caustics. *IEEE Transactions on Visualization and Computer Graphics* 24, 1 (Jan 2018), 984–993. https://doi.org/10.1109/tvcg.2017.2744438

Wilhelm Magnus. 1954. On the exponential solution of differential equations for a linear operator. *Communications on Pure and Applied Mathematics* 7, 4 (1954), 649–673. https://doi.org/10.1002/cpa.3160070404

L. Mandel and E. Wolf. 1995. *Optical Coherence and Quantum Optics*. 1192 pages.

Heylal Mashaal, Alex Goldstein, Daniel Feuermann, and Jeffrey M. Gordon. 2012. First direct measurement of the spatial coherence of sunlight. *Opt. Lett.* 37, 17 (Sep 2012), 3516–3518. https://doi.org/10.1364/OL.37.003516

Michal Mojzík, Tomáš Skřivan, Alexander Wilkie, and Jaroslav Křivánek. 2016. Bi-Directional Polarised Light Transport. In *Eurographics Symposium on Rendering - Experimental Ideas & Implementations*, Elmar Eisemann and Eugene Fiume (Eds.). https://doi.org/10.2312/sre.20161215

Yohei Nishidate. 2013. Closed-form analytical solutions for ray tracing in optically anisotropic inhomogeneous media. *J. Opt. Soc. Am. A* 30, 7 (Jul 2013), 1373–1379. https://doi.org/10.1364/JOSAA.30.001373

Akifumi Ogiwara, Hiroshi Kakiuchida, Masato Tazawa, and Hiroshi Ono. 2007. Analysis of Anisotropic Diffraction Gratings Using Holographic Polymer-Dispersed Liquid Crystal. *Japanese Journal of Applied Physics* 46, 11 (Nov 2007), 7341–7346. https://doi.org/10.1143/jjap.46.7341

J.K. Patel and C.B. Read. 1996. *Handbook of the Normal Distribution, Second Edition*. Taylor & Francis. https://books.google.se/books?id=zoVLF0VF9UYC

Vincent Pegoraro and Steven G. Parker. 2006. Physically-based Realistic Fire Rendering. In *Proceedings of the Second Eurographics Conference on Natural Phenomena (NPH'06)*. Eurographics Association, Goslar Germany, Germany, 51–59. https://doi.org/10.2312/NPH/NPH06/051-059

Kamil Postava, Tomuo Yamaguchi, and Roman Kantor. 2002. Matrix description of coherent and incoherent light reflection and transmission by anisotropic multilayer structures. *Appl. Opt.* 41, 13 (May 2002), 2521–2531. https://doi.org/10.1364/AO.41.002521

Scott A. Prahl. 1995. *The Adding-Doubling Method*. Springer US, Boston, MA, 101–129. https://doi.org/10.1007/978-1-4757-6092-7_5

O. O. Prishchepa, V. Ya. Zyryanov, A. P. Gardymova, and V. F. Shabanov. 2008. Optical Textures and Orientational Structures of Nematic and Cholesteric Droplets with Heterogeneous Boundary Conditions. *Molecular Crystals and Liquid Crystals* 489,

1 (Sep 2008), 84/[410]–93/[419]. https://doi.org/10.1080/15421400802219817
I. Ricardez-Vargas and K. Volke-Sepúlveda. 2010. Experimental generation and dynamical reconfiguration of different circular optical lattices for applications in atom trapping. *Journal of the Optical Society of America B* 27, 5 (Apr 2010), 948. https://doi.org/10.1364/josab.27.000948
Michael Shribak. 2011. Complete polarization state generator with one variable retarder and its application for fast and sensitive measuring of two-dimensional birefringence distribution. *J. Opt. Soc. Am. A* 28, 3 (Mar 2011), 410–419. https://doi.org/10.1364/JOSAA.28.000410
Michael Shribak and Rudolf Oldenbourg. 2003. Techniques for fast and sensitive measurements of two-dimensional birefringence distributions. *Appl. Opt.* 42, 16 (Jun 2003), 3009–3017. https://doi.org/10.1364/AO.42.003009
G. V. Simonenko. 2010. Modelling the optical responses of electrooptic effects of liquid-crystal cells. *Journal of Optical Technology* 77, 2 (Feb 2010), 93. https://doi.org/10.1364/jot.77.000093
Maarten Sluijter, Dick K. de Boer, and H. Paul Urbach. 2009. Ray-optics analysis of inhomogeneous biaxially anisotropic media. *J. Opt. Soc. Am. A* 26, 2 (Feb 2009), 317–329. https://doi.org/10.1364/JOSAA.26.000317
Maarten Sluijter, Dick K. G. de Boer, and Joseph J. M. Braat. 2008. General polarized ray-tracing method for inhomogeneous uniaxially anisotropic media. *J. Opt. Soc. Am. A* 25, 6 (Jun 2008), 1260–1273. https://doi.org/10.1364/JOSAA.25.001260
Alexander Smith, Nicholas L. Abbott, and Victor M. Zavala. 2020. Convolutional Network Analysis of Optical Micrographs. (1 2020). https://doi.org/10.26434/chemrxiv.11688924.v1
S. Stallinga. 1999. Berreman 4X4 matrix method for reflective liquid crystal displays. *Journal of Applied Physics* 85, 6 (1999), 3023–3031. https://doi.org/10.1063/1.369638
Jos Stam and Eric Languénou. 1996. Ray Tracing in Non-Constant Media. In *Rendering Techniques '96*, Xavier Pueyo and Peter Schröder (Eds.). Springer Vienna, Vienna, 225–234.
Holger Stark. 2001. Physics of colloidal dispersions in nematic liquid crystals. *Physics Reports* 351, 6 (Oct 2001), 387–474. https://doi.org/10.1016/s0370-1573(00)00144-7
S. Steinberg. 2019. Analytic Spectral Integration of Birefringence-Induced Iridescence. *Computer Graphics Forum* 38, 4 (jul 2019), 97–110. https://doi.org/10.1111/cgf.13774
Kevin G. Suffern and Phillip H. Getto. 1991. Ray Tracing Gradient Index Lenses. In *Scientific Visualization of Physical Phenomena*, Nicholas M. Patrikalakis (Ed.). Springer Japan, Tokyo, 317–331.
Xin Sun, Kun Zhou, Eric Stollnitz, Jiaoying Shi, and Baining Guo. 2008. Interactive relighting of dynamic refractive objects. In *ACM SIGGRAPH 2008 papers on - SIGGRAPH '08*. ACM Press. https://doi.org/10.1145/1399504.1360634
David C. Tannenbaum, Peter Tannenbaum, and Michael J. Wozny. 1994. Polarization and Birefringency Considerations in Rendering. In *Proceedings of the 21st Annual Conference on Computer Graphics and Interactive Techniques (SIGGRAPH '94)*. 221–222. https://doi.org/10.1145/192161.192204
Volodymyr Tkachenko, Giancarlo Abbate, Antigone Marino, Francesco Vita, Michele Giocondo, Alfredo Mazzulla, Federica Ciuchi, and Luca De Stefano. 2006. Nematic Liquid Crystal Optical Dispersion in the Visible-Near Infrared Range. *Molecular Crystals and Liquid Crystals* 454, 1 (Sep 2006), 263/[665]–271/[673]. https://doi.org/10.1080/15421400600655816
Antoine Toisoul and Abhijeet Ghosh. 2017. Practical Acquisition and Rendering of Diffraction Effects in Surface Reflectance. *ACM Transactions on Graphics* 36, 5 (Jul 2017), 1–16. https://doi.org/10.1145/3012001
Michael Walters, Qianshi Wei, and Jeff Z. Y. Chen. 2019. Machine learning topological defects of confined liquid crystals in two dimensions. *Phys. Rev. E* 99 (Jun 2019), 062701. Issue 6. https://doi.org/10.1103/PhysRevE.99.062701
J. Wei and E. Norman. 1964. On Global Representations of the Solutions of Linear Differential Equations as a Product of Exponentials. *Proc. Amer. Math. Soc.* 15, 2 (1964), 327–334.
Andrea Weidlich and Alexander Wilkie. 2008. Realistic Rendering of Birefringency in Uniaxial Crystals. *ACM Trans. Graph.* 27, 1, Article 6 (March 2008), 12 pages. https://doi.org/10.1145/1330511.1330517
Sebastian Werner, Zdravko Velinov, Wenzel Jakob, and Matthias Hullin. 2017. Scratch Iridescence: Wave-Optical Rendering of Diffractive Surface Structure. *Transactions on Graphics (Proceedings of SIGGRAPH Asia)* 36, 6 (Nov. 2017). https://doi.org/10.1145/3130800.3130840
R. M. Wilcox. 1967. Exponential Operators and Parameter Differentiation in Quantum Physics. *J. Math. Phys.* 8, 4 (1967), 962–982. https://doi.org/10.1063/1.1705306
Yue Wu and Ji-Huan He. 2018. Homotopy perturbation method for nonlinear oscillators with coordinate-dependent mass. *Results in Physics* 10 (Sep 2018), 270–271. https://doi.org/10.1016/j.rinp.2018.06.015
Yunlong Wu, Jinsong Nie, and Li Shao. 2016. Method to measure the phase modulation characteristics of a liquid crystal spatial light modulator. *Applied Optics* 55, 31 (Oct 2016), 8676. https://doi.org/10.1364/ao.55.008676
Ling-Qi Yan, Miloš Hašan, Bruce Walter, Steve Marschner, and Ravi Ramamoorthi. 2018. Rendering Specular Microgeometry with Wave Optics. *ACM Trans. Graph.* 37, 4, Article 75 (July 2018), 10 pages. https://doi.org/10.1145/3197517.3201351
Amnon Yariv and Pochi Yeh. 2003. *Optical waves in crystals : propagation and control of laser radiation.* Hoboken, N.J.: John Wiley and Sons.
Pochi Yeh. 1982. Extended Jones matrix method. *J. Opt. Soc. Am.* 72, 4 (Apr 1982), 507–513. https://doi.org/10.1364/JOSA.72.000507
S.-H. Youn, B.-J. Mun, J. H. Lee, B. K. Kim, H. C. Choi, S. H. Lee, B. Kang, and G.-D. Lee. 2014. Multidimensional calculation of ray path in a twisted nematic liquid crystal cell. *Journal of Modern Optics* 61 (Feb. 2014), 257–262. https://doi.org/10.1080/09500340.2013.879939
Dmitry Zhdanov, Sergey Ershov, Leo Shapiro, Vadim Sokolov, Alexey Voloboy, Vladimir Galaktionov, and Igor Potemin. 2019. Realistic rendering of scenes with anisotropic media. *Optical Engineering* 58, 8 (2019), 1 – 11 – 11. https://doi.org/10.1117/1.OE.58.8.082413
Simon Čopar, Tine Porenta, and Slobodan Žumer. 2013. Visualisation methods for complex nematic fields. *Liquid Crystals* 40, 12 (2013), 1759–1768. https://doi.org/10.1080/02678292.2013.853109 arXiv:https://doi.org/10.1080/02678292.2013.853109

A REPRESENTATION OF THE SOLUTION AS A PRODUCT OF MATRIX EXPONENTIALS

In this appendix we derive the representation of the solution e^{Ω} (equation 29), as well as the scalar ODEs that accompany it (equations 25-28).

We start with a few preliminaries. Let $\mathrm{A}, \mathrm{B} \in \mathfrak{gl}_n$, where $\mathfrak{gl}_n$ is the general Lie algebra consisting of $n \times n$ real matrices, then the Lie bracket is the matrix commutator defined as $[\mathrm{A}, \mathrm{B}] = \mathrm{AB} - \mathrm{BA}$. For convenience we also define the *adjoint* linear operator $\mathrm{ad}_{\mathrm{A}}\,\mathrm{B} = [\mathrm{A}, \mathrm{B}]$, then $\mathrm{ad}^2_{\mathrm{A}}\,\mathrm{B} = [\mathrm{A}, [\mathrm{A}, \mathrm{B}]]$ and so on. The matrix exponential maps $\mathfrak{gl}_n$ to its Lie group $GL_n(\mathbb{R})$ via the series expansion

$$e^{\mathrm{A}} = \mathrm{I} + \mathrm{A} + \frac{\mathrm{A}^2}{2!} + \frac{\mathrm{A}^3}{3!} + \cdots = \sum_{m=0}^{\infty} \frac{\mathrm{A}^m}{m!} \tag{39}$$

and note that the identity $e^{\mathrm{A}+\mathrm{B}} = e^{\mathrm{A}} e^{\mathrm{B}}$ holds only when A, B commute (that is $[\mathrm{A}, \mathrm{B}] = 0$). We also define the operator $e^{\mathrm{ad}_{\mathrm{A}}}$ which when acting upon a Lie algebra element can be rewritten as a series using the Baker-Hausdorff formula:

$$e^{\mathrm{ad}_{\mathrm{A}}}\mathrm{B} = e^{\mathrm{A}}\mathrm{B}e^{-\mathrm{A}} = \mathrm{B} + \mathrm{ad}_{\mathrm{A}}\,\mathrm{B} + \frac{1}{2!}\,\mathrm{ad}^2_{\mathrm{A}}\,\mathrm{B} + \cdots \tag{40}$$

The Magnus expansion [Magnus 1954] can be considered as the continuous analog of the Baker-Campbell-Hausdorff formula (given an equation $e^{\mathrm{X}} = e^{\mathrm{A}+\mathrm{B}}$ the BCH formula provides an infinite series expansion to the matrix X that solves the equation for small enough A and B) and provides a local representation of the solution to a first-order ordinary differential equation that involves a linear operator. Specifically, the solution to the differential equation 19 can be represented by a matrix exponent e^{Ω} of an infinite sum $\Omega(y) = \sum_{m=1}^{\infty} \Delta_m(y)$ in some neighbourhood of $y = 0$ such that $\psi(y) = e^{\Omega(y)}\psi(0)$ [Wilcox 1967]. The first couple of terms of Ω are

$$\begin{aligned} \Delta_1(y) &= \int_0^y \boldsymbol{\mathcal{A}}(\xi)\,\mathrm{d}\xi \\ \Delta_2(y) &= \frac{1}{2}\int_0^y \int_0^{\xi} [\boldsymbol{\mathcal{A}}(\xi), \boldsymbol{\mathcal{A}}(h)]\,\mathrm{d}h\,\mathrm{d}\xi \end{aligned} \tag{41}$$

subsequent terms are computed recursively and involve additional nested integrals of nested commutators. If $\boldsymbol{\mathcal{A}}$ were to commute with itself all the commutators would vanish and e^{Ω} would be reduced to the well-known classical solution to the matrix-valued differential equation, viz. $e^{\Omega} = \exp\left(\int_0^y \boldsymbol{\mathcal{A}}(\xi)\,\mathrm{d}\xi\right)$. What follows is a direct result of the Magnus expansion:

Lemma A.1. *When the linear operator is expressed as a linear combination of Lie algebra elements, viz.* $\boldsymbol{\mathcal{A}}(y) = \sum_{j=1}^{m} a_j(y)\,\mathrm{X}_j$ *(with the* X_j *being independent of* y*), the solution can also be written as a linear combination of the same elements due to the closure property of Lie algebras. That is, if* $\mathfrak{g}$ *is the Lie algebra generated by* $\{\mathrm{X}_1, \cdots, \mathrm{X}_m\}$*, then* $\mathrm{ad}^m_{\boldsymbol{\mathcal{A}}(y_1)}\boldsymbol{\mathcal{A}}(y_2) \in \mathfrak{g}$ *for any* $m \geq 0$ *and* $y_1, y_2 \in [0, -\tau]$*, therefore* $\Delta_j \in \mathfrak{g}$ *and as a consequence*

$$e^{\Omega(y)} = \prod_{j=1}^{m} e^{f_j(y)\mathrm{X}_j}$$

Proof given by Wilcox [1967]. □

Under the conditions of Lemma A.1 the following Lemma was proven by Wei and Norman [1964]:

Lemma A.2. *Given* $\boldsymbol{\mathcal{A}}$ *and* $\mathfrak{g}$ *as above, it holds that* e^{Ω} *can be represented as a product of matrix exponentials, viz.* $e^{\Omega(y)} = \prod_{j=1}^{m} e^{f_j(y)\mathrm{X}_j}$*. Furthermore the scalar functions* $f_j(y)$ *depend only on the scalar functions* $a_j(y)$ *as well as the Lie algebra* $\mathfrak{g}$ *via the following relation*

$$\sum_{j=1}^{m} a_j(y)\,\mathrm{X}_j = \sum_{j=1}^{m} \frac{\mathrm{d}f_j(y)}{\mathrm{d}y}\left[\prod_{l=1}^{j-1} e^{f_l(y)\,\mathrm{ad}_{\mathrm{X}_l}}\right]\mathrm{X}_j$$

Lemma A.2 produces a system of ODEs, a system that can always be solved numerically by quadrature. We are interested, however, in an analytic solution or approximation to e^{Ω} that is adequate for use in the context of computer rendering. To that end, the elements X_j are selected such that the system simplifies into linear and quadratic first-order ODEs only:

$$\mathrm{X}_1 = \begin{bmatrix} 0 & 1 \\ 0 & 0 \end{bmatrix} \quad \mathrm{X}_2 = \begin{bmatrix} 0 & 0 \\ 1 & 0 \end{bmatrix} \quad \mathrm{X}_3 = \begin{bmatrix} 1 & 0 \\ 0 & -1 \end{bmatrix} \quad \mathrm{X}_4 = \mathrm{I} \tag{42}$$

and the Lie multiplication table that emerges for $\mathrm{X}_{1,2,3}$ is then

$$[\mathrm{X}_1, \mathrm{X}_2] = \mathrm{X}_3 \quad [\mathrm{X}_1, \mathrm{X}_3] = -2\mathrm{X}_1 \quad [\mathrm{X}_2, \mathrm{X}_3] = 2\mathrm{X}_2 \tag{43}$$

We rewrite $\boldsymbol{\mathcal{A}}(y) = a(y)\,\mathrm{I} + \mathrm{B}(y)$, with $\mathrm{B}(y) = \sum_{j=1}^{3} b_j(y)\,\mathrm{X}_j$, such that the functions $a(y)$, $b_{1,2,3}(y)$ satisfy equation 20. The solution can then be represented via the following corollary:

Corollary A.2.1. *Given* $\mathrm{X}_1, \mathrm{X}_2, \mathrm{X}_3$ *and* $\boldsymbol{\mathcal{A}}$ *as defined above the representation of the solution* e^{Ω} *takes the form*

$$e^{\Omega} = e^{f(y)\mathrm{I}} \prod_{j=1}^{3} e^{g_j(y)\mathrm{X}_j}$$

with $f(y) = \int_0^y a(\xi)\,\mathrm{d}\xi$*, and* $u(y) = \prod_{j=1}^{3} e^{g_j(y)\mathrm{X}_j}\psi(0)$ *being the solution to the differential equation* $\mathrm{d}u/\mathrm{d}y = \mathrm{B}u$ *accompanied by the boundary condition* $u(0) = \psi(0)$*.*

Proof. By Lemma A.1 the solution can be represented as a product of matrix exponentials. Then, it is easy to see that

$$\frac{\mathrm{d}}{\mathrm{d}y}(e^{f\mathrm{I}}u) = \left(\frac{\mathrm{d}}{\mathrm{d}y}e^{f\mathrm{I}}\right)u + e^{f\mathrm{I}}\frac{\mathrm{d}u}{\mathrm{d}y} = (a\mathrm{I} + \mathrm{B})\,e^{f\mathrm{I}}u$$

Therefore $u = e^{-f\mathrm{I}}\psi$ and indeed $\psi = e^{f\mathrm{I}}u$. □

We will now derive the differential equations system for the functions $g_{1,2,3}$ in the representation of the solution for $u = e^{-f\mathrm{I}}\psi$. The Lie algebra $\mathfrak{g}$ is then generated by $\{\mathrm{X}_1, \mathrm{X}_2, \mathrm{X}_3\}$ and we proceed by directly applying Lemma A.2:

$$\begin{aligned} &b_1\mathrm{X}_1 + b_2\mathrm{X}_2 + b_3\mathrm{X}_3 = \\ &= \frac{\mathrm{d}g_1}{\mathrm{d}y}\mathrm{X}_1 + \frac{\mathrm{d}g_2}{\mathrm{d}y}e^{g_1\,\mathrm{ad}_{\mathrm{X}_1}}\mathrm{X}_2 + \frac{\mathrm{d}g_3}{\mathrm{d}y}e^{g_1\,\mathrm{ad}_{\mathrm{X}_1}}e^{g_2\,\mathrm{ad}_{\mathrm{X}_2}}\mathrm{X}_3 = \\ &= \frac{\mathrm{d}g_1}{\mathrm{d}y}\mathrm{X}_1 + \frac{\mathrm{d}g_2}{\mathrm{d}y}\left(\mathrm{X}_2 + g_1\mathrm{X}_3 - g_1^2\mathrm{X}_1\right) + \\ &\quad + \frac{\mathrm{d}g_3}{\mathrm{d}y}\left[\mathrm{X}_3 - 2g_1\mathrm{X}_1 + 2g_2\left(\mathrm{X}_2 + g_1\mathrm{X}_3 - g_1^2\mathrm{X}_1\right)\right] \end{aligned} \tag{44}$$

where we applied the Baker-Hausdorff formula (eq. 40) using the multiplication table 43. Equating the X_j on each side results in the system

$$\begin{aligned} \begin{bmatrix} b_1 \\ b_2 \\ b_3 \end{bmatrix} &= \mathrm{G}\,\frac{\mathrm{d}}{\mathrm{d}y}\begin{bmatrix} g_1 \\ g_2 \\ g_3 \end{bmatrix} = \\ &= \begin{bmatrix} 1 & -g_1^2 & -2g_1(1 + g_1g_2) \\ 0 & 1 & 2g_2 \\ 0 & g_1 & 1 + 2g_1g_2 \end{bmatrix}\frac{\mathrm{d}}{\mathrm{d}y}\begin{bmatrix} g_1 \\ g_2 \\ g_3 \end{bmatrix} \end{aligned} \tag{45}$$

which always has a unique solution as the determinant $\det(\mathrm{G}) = 1$ never vanishes. This gives rise to three ODEs:

$$\frac{\mathrm{d}}{\mathrm{d}y}g_1 = -b_2g_1^2 + 2b_3g_1 + b_1 \tag{46}$$

$$\frac{\mathrm{d}}{\mathrm{d}y}g_2 = 2(g_1b_2 - b_3)\,g_2 + b_2 \tag{47}$$

$$\frac{\mathrm{d}}{\mathrm{d}y}g_3 = -b_2g_1 + b_3 \tag{48}$$

with initial conditions $g_1(0) = g_2(0) = g_3(0) = 0$. The first non-linear ODE, for g_1, is known as the *Riccati equation* [Ric 1972], which reduces to a second-order linear ODE and could be solved analytically if a particular solution was to be found, e.g., by an ansatz. g_2 is a linear first-order ODE and its general solution takes the well-known form

$$\begin{aligned} g_2(y) &= e^{-\mu(y)}\int_0^y e^{\mu(\xi)}b_2(\xi)\,\mathrm{d}\xi \\ \mu(y) &= -2\int_0^y \left[g_1(\xi)\,b_2(\xi) - b_3(\xi)\right]\mathrm{d}\xi \end{aligned} \tag{49}$$

The ODE for g_3 is separable therefore its solution is found simply by integration.

Finally, using corollary A.2.1 and observing that $\mathrm{X}_1, \mathrm{X}_2$ are nilpotent while X_3, I are diagonal, we can compute the matrix exponentials and write the representation for the solution e^{Ω} as

$$\begin{aligned} e^{\Omega} = e^{f\mathrm{I}}\prod_{j=1}^{3} e^{g_j\mathrm{X}_j} &= e^{f}\,(\mathrm{I} + g_1\mathrm{X}_1)\,(\mathrm{I} + g_2\mathrm{X}_2)\begin{bmatrix} e^{g_3} & \\ & e^{-g_3} \end{bmatrix} = \\ &= e^{f}\begin{bmatrix} (1 + g_1g_2)\,e^{g_3} & g_1e^{-g_3} \\ g_2e^{g_3} & e^{-g_3} \end{bmatrix} \end{aligned} \tag{50}$$

where $f(y) = \int_0^y a(\xi)\,\mathrm{d}\xi$.

This completes the derivation of equations 25-29.

A note regarding convergence. The representation provided by the Magnus expansion is generally confined to a local neighbourhood. However, as the determinant of G never vanishes and the functions a, b_1, b_2, b_3 are analytic the general solution to equation 19 is provided by 50 and the representation is global [Wei and Norman 1964].

Basis choice. The choice of the basis X_1, X_2, X_3 is motivated by producing a tractable system G (eq. 45). Note that the order of the basis elements is also crucial (as can be seen from Lemma A.2). Ideally the resulting system should posses the following characteristics:

(1) Non-vanishing determinant $\det(\mathrm{G})$.
(2) The resulting ODEs (eq. 25-27) should not give rise to circular inter-dependencies (in which case the system reduces back to an operator-valued ODE).
(3) Finally, we would like the ODEs to have analytic solutions, admit acceptable analytic approximations or be well-behaved enough for semi-analytic methods.

Our basis of choice was produced by a combination of trial-and-error and analytic methods and it satisfies the first two requirements fully. The Riccati ODE for g_1 does not admit a general solution form, however, as will be seen in the next subsection, this is a non-issue.

B ANALYTIC REPRESENTATIONS FOR f AND $g_{1,2,3}$

In this appendix we approximate the scalar functions f, g_1, g_2 and g_3 (equations 25-28) with analytic expressions to derive the final closed-form equations 30-33.

Simplifications. Note that b_1 and b_2 are the cross-component (ordinary to extraordinary and vice versa) terms in the operator $\boldsymbol{\mathcal{A}}$ (equation 20) and by our assumption of slowly varying optical constants we can deduce that $|b_1|, |b_2| \ll 1$. As $g_1(0) = 0$, and therefore $\left|\frac{\mathrm{d}}{\mathrm{d}y} g_1(0)\right| \ll 1$, there is a region around $y = 0$ where $|g_1| \ll 1$ and in that region $b_2 g_1^2 \approx 0$. The Riccati ODE for g_1 then simplifies to

$$\frac{\mathrm{d}}{\mathrm{d}y} g_1 = 2b_3 g_1 + b_1 \tag{51}$$

and using similar arguments we can also simplify g_2 equivalently:

$$\frac{\mathrm{d}}{\mathrm{d}y} g_2 = -2b_3 g_2 + b_2 \tag{52}$$

Furthermore, observe that as $\mathrm{Im}\{b_1\} \equiv 0$, by construction, it holds that

$$\forall n \in \mathbb{N} \to \mathrm{Im}\{\frac{\mathrm{d}^n}{\mathrm{d}y^n} g_1(0)\} = 0$$

therefore we can assume that $\mathrm{Im}\{g_1\} \approx 0$ in some neighbourhood of $y = 0$ and it follows that

$$\mathrm{Im}\left\{\frac{\mathrm{d}}{\mathrm{d}y} g_3\right\} = -b_2 \,\mathrm{Im}\{g_1\} + \mathrm{Im}\{b_3\} \approx \mathrm{Im}\{b_3\} \tag{53}$$

It then becomes worthwhile to rewrite the ODE for g_3 entirely as:

$$\frac{\mathrm{d}}{\mathrm{d}y} g_3 = b_3 \tag{54}$$

The justification is that clearly $|b_2 g_1| \ll 1$ and therefore the errors in the real part of g_3 would be small, and because of the $k = \frac{2\pi}{\lambda}$ (the wavenumber) factor in the imaginary parts of $b_{1,2,3}$ (see eq. 20), which is very large for wavelengths in the visible spectrum, the solution is significantly more sensitive to errors in the imaginary parts than the real parts.

Note that the simplified ODEs are now completely independent from each other. When deriving analytic expressions for the solution e^{Ω}, this fact can allow us to approximate different elements of the solution with varying precision. For example, as discussed in section 4, f and g_3, especially their imaginary parts, have special meaning and carry crucial information. As f and g_3 have been reduced to very simple separable ODEs, they could be computed with greater accuracy, or even with a closed-form solution, while the more complicated functions g_1, g_2 could be approximated in a more lax manner (e.g., in order to reduce computation time). This is generally not possible with methods that aim to approximate the radiative transfer differential equation (eq. 19) directly.

The analytic forms of the solutions to the simplified ODEs are then

$$g_1(y) = e^{\mu(y)} \int_0^y e^{-\mu(\xi)} b_1(\xi)\,\mathrm{d}\xi \tag{55}$$

$$g_2(y) = e^{-\mu(y)} \int_0^y e^{\mu(\xi)} b_2(\xi)\,\mathrm{d}\xi \tag{56}$$

$$g_3(y) = \int_0^y b_3(\xi)\,\mathrm{d}\xi \tag{57}$$

$$f(y) = \int_0^y a(\xi)\,\mathrm{d}\xi \tag{58}$$

with

$$\mu(y) = \int_0^y 2b_3(\xi)\,\mathrm{d}\xi = 2g_3$$

See figure 12 for plots that compare numerically differentiated solutions to the simplified ODEs against solutions to the full ODEs (listed in equations 25-27) for a sample material. As expected, accuracy remains high in practice and for the rest of the paper we use the simplified ODEs for $g_{1,2,3}$, as defined in this subsection.

Analytic solutions for g_1, g_2 using Gaussian integrals. The integrals in the solutions to the functions g_1, g_2 (equations 55-56) generally do not admit a closed-form solution. We approximate those integrals via a sum of Gaussian integrals, i.e. integrals that are of the form $\int_0^x \phi(\xi)\,\xi^n\,\mathrm{d}\xi$, for some non-negative integer n and with the ϕ being the Gaussian distribution's PDF (probability distribution function):

$$\phi(x) = \frac{1}{\sqrt{2\pi}} e^{-\frac{x^2}{2}} \tag{59}$$

When $n = 0$ the Gaussian integral is the CDF (cumulative distribution function), which defines the *standard error function*, erf:

$$\int_0^x \phi(\xi)\,\mathrm{d}\xi = \sqrt{\frac{\pi}{2}}\,\mathrm{erf}\left(\frac{x}{\sqrt{2}}\right) \tag{60}$$

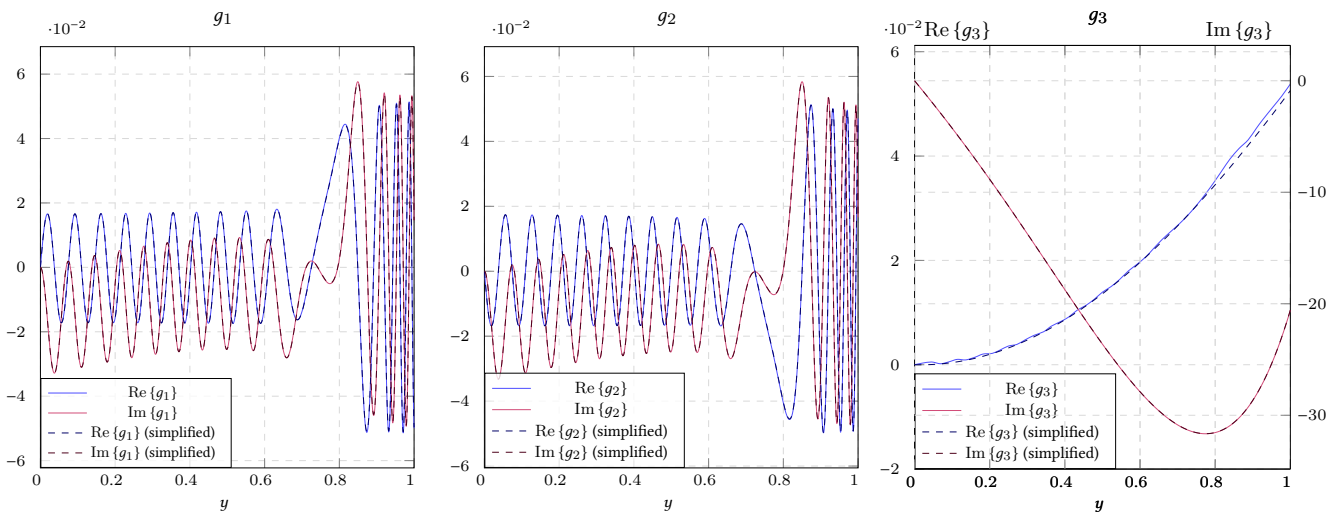

Fig. 12. Comparison between solutions to the ODEs (eq. 25-27) and the simplified ones, obtained via a numerical solver. Blue and violet plots are the real and imaginary parts, respectively, of the solution of the full ODEs ("ground-truth"), while the dashed black plots are the simplified versions. With the exception of the real part of g_3, which introduces small errors, the solutions to the simplified ODEs are identical for all practical intents and purposes. The numerical solutions were generated using the evaluation slab (see section 5.3), with $K = \frac{\pi}{8}$ and $\lambda = 500\,\mathrm{nm}$.

For $n > 0$ a recursive relation is trivially deduced via integration by parts:

$$\int_0^x \phi(\xi)\,\xi\,\mathrm{d}\xi = -\phi(x) + \frac{1}{\sqrt{2\pi}} \tag{61}$$

$$\int_0^x \phi(\xi)\,\xi^{n+2}\,\mathrm{d}\xi = -x^{n+1}\phi(x) + (n+1)\int_0^x \phi(\xi)\,\xi^n\,\mathrm{d}\xi \tag{62}$$

the recursive relation is then easily reduced to the closed-form equations 36 [Patel and Read 1996].

A closely related integral of the form $\int_0^x \phi(\alpha+\beta\xi)\,\xi^n\,\mathrm{d}\xi$, for some constants $\alpha, \beta \in \mathbb{C}$, reduces to a sum of Gaussian integrals by a change of variable $u = \alpha + \beta\xi$ and an application of the Binomial theorem:

$$\int_0^x \phi(\alpha+\beta\xi)\,\xi^n\,\mathrm{d}\xi = \frac{1}{\beta^{n+1}}\sum_{m=0}^{n}\binom{n}{m}(-\alpha)^{n-m}\left[\int_0^{\alpha+\beta x} u^m\phi(u)\,\mathrm{d}u - \int_0^{\alpha} u^m\phi(u)\,\mathrm{d}u\right] \tag{63}$$

Finally, we also define the Taylor expansion operator $\mathcal{T}_n$, which expands an input $f(x)$ into its n^{th}-order Taylor series around the point $x = 0$:

$$\mathcal{T}_n\{f\}(x) = \sum_{m=0}^{n}\frac{x^m}{m!}\frac{\mathrm{d}^m}{\mathrm{d}x^m}f(0) \tag{64}$$

We turn our attention back to the solution forms of g_1 and g_2. Observe that the real part of g_3, as well as b_1 and b_2, are small and well-behaved, by the assumption of slowly varying optical properties. The imaginary part of g_3, however, grows rapidly due to the wavenumber factor, as discussed previously. Then, the integrand of the solutions of g_1, g_2 can be rewritten by factoring out the highly oscillatory term that arises due to $\mathrm{Im}\{g_3\}$:

$$g_1(y) = e^{2g_3(y)}\int_0^y e^{-2i\,\mathrm{Im}\{g_3(\xi)\}}\cdot\left(e^{-2\,\mathrm{Re}\{g_3(\xi)\}}b_1(\xi)\right)\mathrm{d}\xi \tag{65}$$

(with similar expression for g_2). The right-hand side term in the integrand, $e^{-2\,\mathrm{Re}\{g_3\}}b_1$, is then well behaved and can be represented by its truncated Taylor series. As the imaginary part of g_3 carries the phase difference, it tends to be very smooth in practice and can be approximated by a quadratic function reasonably well (see figure 13). Then, the solutions of g_1, g_2 are approximated via sums of Gaussian integrals:

$$g_1(y) \approx \sqrt{2\pi}\cdot e^{2g_3(y)-\frac{\alpha^2}{2}}\cdot \cdot\int_0^y \phi(i\alpha+i\beta\xi)\,\mathcal{T}_n\left\{e^{-2\,\mathrm{Re}\{g_3(\xi)\}}b_1(\xi)\right\}\mathrm{d}\xi \tag{66}$$

$$g_2(y) \approx \sqrt{2\pi}\cdot e^{-2g_3(y)+\frac{\alpha^2}{2}}\cdot \cdot\int_0^y \phi(\alpha+\beta\xi)\,\mathcal{T}_n\left\{e^{2\,\mathrm{Re}\{g_3(\xi)\}}b_2(\xi)\right\}\mathrm{d}\xi \tag{67}$$

with the expansion order n being chosen a priori. Given the series coefficients $c_1, c_2 \in \mathbb{R}$ such that

$$\mathcal{T}_2\{\mathrm{Im}\{g_3(y)\}\} = c_1 y + c_2 y^2$$

the constants α and β that satisfy $-\frac{(\alpha+\beta y)^2}{2} + \frac{\alpha^2}{2} = 2i\left(c_1 y + c_2 y^2\right)$ are then

$$\alpha = \frac{(1-i)\,c_1}{\sqrt{2c_2}} \qquad \beta = (1-i)\sqrt{2c_2} \tag{68}$$

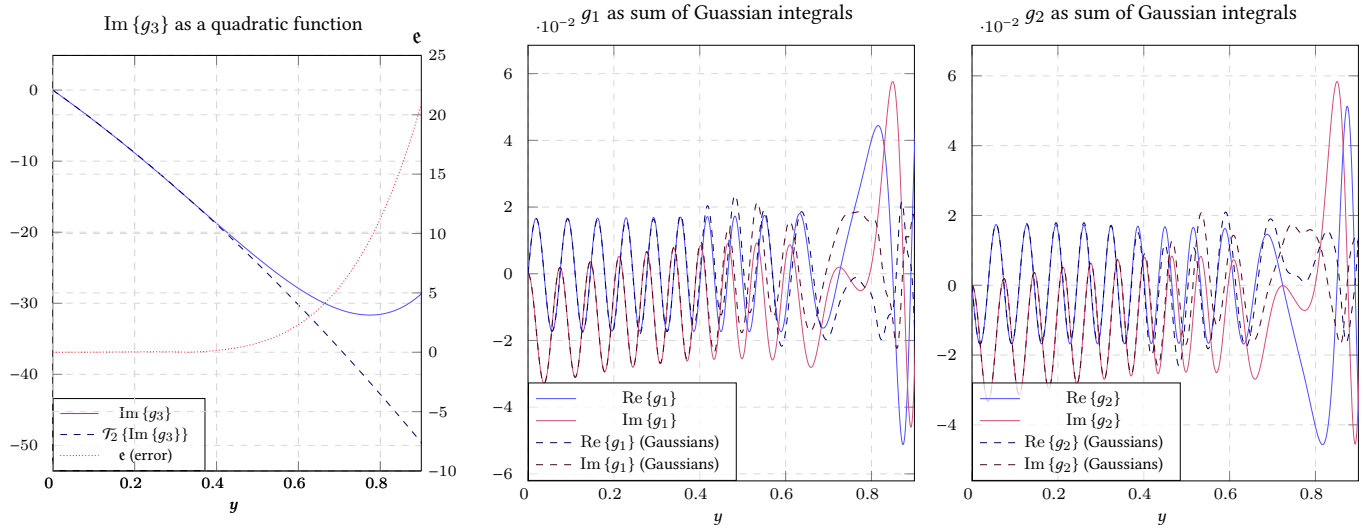

Fig. 13. Approximate analytic closed-form expressions for the solutions to the differential equations for g_1 and g_2. We approximate the imaginary part of g_3 by a quadratic function $\mathcal{T}_2\{\mathrm{Im}\{g_3\}\}$ (its second-order Taylor expansion) and use that function to rewrite the solutions to g_1 and g_2 (eq. 55-56) as a sum of Gaussian integrals, in which case the solutions become analytical expressions that involve the complex error function. The resulting solutions are highly precise as long as $\mathrm{Im}\{g_3\}$ can be accurately represented by $\mathcal{T}_2\{\mathrm{Im}\{g_3\}\}$. We quantify the error via the function $\mathfrak{e} = |\mathrm{Im}\{g_3 - \mathcal{T}_2\{g_3\}\}|$ (plotted on the left), which expresses the phase error in the complex exponent term of the integrands in equations 55, 56. When $\mathfrak{e} < \frac{\pi}{2}$, that is less than a quarter of a phase cycle, the solutions are considered to be very accurate.

See figure 13 for plots of the resulting expressions for g_1, g_2 and comparison against the numerically differentiated solutions of the full ODEs.

Analytic expressions for f and g_3. Finding a closed-form solution for the integrals for f and g_3 (eq. 57-58) might be infeasible in practice—the operator $\boldsymbol{\mathcal{A}}$ is usually complicated and depends on the user-supplied functions for the optical properties. We then choose to also use the Taylor series of the functions a and b_3 for the computations of f and g_3:

$$g_3(y) \approx \int_0^y \mathcal{T}_n\{b_3(\xi)\}\,\mathrm{d}\xi \qquad f(y) \approx \int_0^y \mathcal{T}_n\{a(\xi)\}\,\mathrm{d}\xi \tag{69}$$

As a and b_3 tend to be very smooth, this does not affect the accuracy of the method, which in practice remains limited by the approximations for g_1, g_2.

Alternative methods. It is worth noting that some semi-analytic methods can at times produce better results compared to the technique described in this appendix. A method that is flexible enough to deal with the highly oscillatory nature of g_1 and g_2 is the *Homotopy Perturbation Method* (HPM) [He 1999; Wu and He 2018], which is a powerful technique that has been successfully applied to a variety of non-linear partial and ordinary differential equations. Using HPM we have successfully obtained good approximations of the functions g_1 and g_2 for some inputs, however choosing the basis functions of the solution space is non-trivial and the resulting expressions tend to diverge rapidly on other inputs. In general, our presented method produces better results, remains stable on a wide range of inputs and does not require any manual configuration. All of our presented results (see section 5) have been accomplished by using the method as described.

C ELECTRIC FIELDS AND WAVEVECTORS

The required equations for light propagation in an uniaxial medium are provided here. The full expressions for the Fresnel coefficients for isotropic-to-anisotropic and anisotropic-to-isotropic interfaces, as well as the general anisotropic-to-anisotropic interface, are too long to list here and are provided in full in our supplemental material (as MATLAB™ scripts). See [Steinberg 2019] for more details.

Given the incidence parameter $K = \eta \sin\theta$ (equation 8), the normal modes, i.e. the components of the wave's direction of propagation normal to the interface (the y-component), become:

$$\begin{aligned} q_o^{\pm} &= \pm\sqrt{\hat{\epsilon}_o - K^2} \\ q_e^{\pm} &= \frac{\pm\sqrt{\hat{\epsilon}_o}\sqrt{\hat{\epsilon}_e\left(\beta^2\Delta\epsilon + \hat{\epsilon}_o\right) + K^2\left(\alpha^2\Delta\epsilon - \hat{\epsilon}_e\right)} + \beta\gamma K\Delta\epsilon}{\hat{\epsilon}_o + \beta^2\Delta\epsilon} \end{aligned} \tag{70}$$

where $\hat{\epsilon}_{o,e}$ are the ordinary and extraordinary permittivities, $\Delta\epsilon = \hat{\epsilon}_e - \hat{\epsilon}_o$ and $\vec{\mathfrak{a}} = [\,\alpha,\beta,\gamma\,]^T$ is the optic axis. The subscript denotes an ordinary or extraordinary wave, while a positive sign in the superscript denotes a ray propagating upwards and a minus sign indicates downwards. The (unnormalized) wave's direction of propagation is then

$$\vec{\mathrm{w}}_{o,e}^{\pm} = \left[0, q_{o,e}^{\pm}, -K\right]^T \tag{71}$$

and the electric fields for the relevant waves are given by

$$\vec{\mathrm{E}}_o^{\pm} = \frac{1}{N_o^{\pm}} \left(\vec{\mathrm{a}} \times \vec{\mathrm{w}}_o^{\pm}\right) \qquad \vec{\mathrm{E}}_e^{\pm} = \frac{1}{N_e^{\pm}} \left[\hat{\epsilon}_o \vec{\mathrm{a}} + \left(\gamma K - \beta q_e^{\pm}\right) \vec{\mathrm{w}}_e^{\pm}\right]$$

with $N_{o,e}^{\pm}$ being the normalization factors. Finally, a wave's phase velocity direction and wavevector are simply [Born and Wolf 1999]:

$$\vec{\mathrm{s}} = \frac{\vec{\mathrm{w}}}{|\vec{\mathrm{w}}|} \qquad \vec{\mathrm{k}} = k\vec{\mathrm{s}} \tag{72}$$

where $k = \frac{2\pi}{\lambda}$ is defined as the wavenumber.

As the incidence parameter K remains constant for all participating waves, the effective (real) refractive-index perceived by a wave propagating in an anisotropic media is [Yariv and Yeh 2003]

$$\eta_{\mathrm{ef}} = \frac{K}{\sin\phi} = \sqrt{q^2 + K^2} \tag{73}$$

with ϕ being the wave's angle of refraction or reflection, and for an extraordinary wave η_{ef} varies between ϵ_o and ϵ_e.

D CONSTRAINTS ON THE INCIDENCE PARAMETER

The *maximal incidence parameter*, closely related to the critical angle, is defined as

$$K_e^{\max} = \eta_e \sqrt{\frac{\eta_o^2 + \beta^2 \Delta\epsilon}{\eta_e^2 - \gamma^2 \Delta\epsilon}} \qquad K_o^{\max} = \eta_o \tag{74}$$

When $K \geq K^{\max}$ total-reflection occurs: The refracted wave becomes evanescent and its associated Poynting vector—the direction of the electromagnetic flux—is complex and parallel to the surface interface. For our assumption of no total-reflection happening in the slab to hold, we need to enforce that

$$K \leq \inf\left\{K_e^{\max}(y), K_o^{\max}(y) \mid y \in [0, -\tau]\right\} \tag{75}$$

In addition, we also would like to be able to enforce adherence to a predefined coherence size by setting an upper bound on $\bar{c}$, the length of the participating part of incident wavefront (see figure 2). This is done by limiting the incidence angle of the incident plane-wave. The maximal horizontal offset between participating waves in the slab is

$$\mathfrak{h} = \int_0^y \left| \frac{\left(\vec{\mathrm{s}}_e(\xi)\right)_z}{\left(\vec{\mathrm{s}}_e(\xi)\right)_y} - \frac{\left(\vec{\mathrm{s}}_o(\xi)\right)_z}{\left(\vec{\mathrm{s}}_o(\xi)\right)_y} \right| \mathrm{d}\xi \tag{76}$$

and the projected size of this offset onto the incident wavefront is $l = \frac{\mathfrak{h}}{\cos\theta}$ therefore the maximal incidence angle such that $l \leq \bar{c}$ is

$$\theta^{\max} = \cos^{-1}\left(\frac{\mathfrak{h}}{\bar{c}}\right) \tag{77}$$

Note that when $\frac{\mathfrak{h}}{\bar{c}} > 1$ this constraint can not be satisfied for the given slab.

E FRESNEL COEFFICIENTS FOR A THIN ANISOTROPIC SLAB

By the boundary conditions implied by Maxwell's equations, the tangential components of the electric fields $\vec{\mathrm{E}}$ are continuous across an interface between two media [Born and Wolf 1999], allowing us to deduce the Fresnel coefficients at that interface by taking into account all participating electric fields—the incident and the reflected fields on one side, and the refracted field on the other side. This gives rise to a system of 4 independent equations with 4 unknown, and in our supplemental material we provide the solution for the general case of an anisotropic-to-anisotropic interface.

However, as we have assumed negligible back-reflections, equating the reflected field to zero vastly simplifies the systems and we are left with the following two systems: One for an incident ordinary field; and one for an incident extraordinary field. For succinctness we denote the short-hands $\vec{\mathrm{x}}_{o,e} = (\vec{\mathrm{E}}_{o,e})_x$ and $\vec{\mathrm{z}}_{o,e} = (\vec{\mathrm{E}}_{o,e})_z$ and the systems become:

$$\begin{cases} \vec{\mathrm{x}}_o(y) = t_{oo}\vec{\mathrm{x}}_o(y + \Delta y) + t_{oe}\vec{\mathrm{x}}_e(y + \Delta y) \\ \vec{\mathrm{z}}_o(y) = t_{oo}\vec{\mathrm{z}}_o(y + \Delta y) + t_{oe}\vec{\mathrm{z}}_e(y + \Delta y) \end{cases} \tag{78}$$

$$\begin{cases} \vec{\mathrm{x}}_e(y) = t_{eo}\vec{\mathrm{x}}_o(y + \Delta y) + t_{ee}\vec{\mathrm{x}}_e(y + \Delta y) \\ \vec{\mathrm{z}}_e(y) = t_{eo}\vec{\mathrm{z}}_o(y + \Delta y) + t_{ee}\vec{\mathrm{z}}_e(y + \Delta y) \end{cases} \tag{79}$$

Solving those systems yields the transmission coefficients for our slab of thickness Δy:

$$\begin{aligned} t_{oo} &= \frac{\vec{\mathrm{z}}_o(y)\,\vec{\mathrm{x}}_e(y + \Delta y) - \vec{\mathrm{x}}_o(y)\,\vec{\mathrm{z}}_e(y + \Delta y)}{N_t} \\ t_{eo} &= \frac{\vec{\mathrm{z}}_e(y)\,\vec{\mathrm{x}}_e(y + \Delta y) - \vec{\mathrm{x}}_e(y)\,\vec{\mathrm{z}}_e(y + \Delta y)}{N_t} \\ t_{oe} &= \frac{\vec{\mathrm{x}}_o(y)\,\vec{\mathrm{z}}_o(y + \Delta y) - \vec{\mathrm{z}}_o(y)\,\vec{\mathrm{x}}_o(y + \Delta y)}{N_t} \\ t_{ee} &= \frac{\vec{\mathrm{x}}_e(y)\,\vec{\mathrm{z}}_o(y + \Delta y) - \vec{\mathrm{z}}_e(y)\,\vec{\mathrm{x}}_o(y + \Delta y)}{N_t} \end{aligned} \tag{80}$$

with

$$N_t = \vec{\mathrm{x}}_e(y + \Delta y)\,\vec{\mathrm{z}}_o(y + \Delta y) - \vec{\mathrm{x}}_o(y + \Delta y)\,\vec{\mathrm{z}}_e(y + \Delta y) \tag{81}$$

Differentiating and taking the limit gives us the coefficients that appear in operator $\boldsymbol{\mathcal{A}}$ (eq. 20):

$$\begin{aligned} \dot{t}_{oo} &= \frac{1}{N_t}\bigg|_{\Delta y=0} \left[\vec{\mathrm{z}}_e(y)\frac{d}{dy}\vec{\mathrm{x}}_o(y) - \vec{\mathrm{x}}_e(y)\frac{d}{dy}\vec{\mathrm{z}}_o(y)\right] \\ \dot{t}_{eo} &= \frac{1}{N_t}\bigg|_{\Delta y=0} \left[\vec{\mathrm{z}}_e(y)\frac{d}{dy}\vec{\mathrm{x}}_e(y) - \vec{\mathrm{x}}_e(y)\frac{d}{dy}\vec{\mathrm{z}}_e(y)\right] \\ \dot{t}_{oe} &= \frac{1}{N_t}\bigg|_{\Delta y=0} \left[\vec{\mathrm{x}}_o(y)\frac{d}{dy}\vec{\mathrm{z}}_o(y) - \vec{\mathrm{z}}_o(y)\frac{d}{dy}\vec{\mathrm{x}}_o(y)\right] \\ \dot{t}_{ee} &= \frac{1}{N_t}\bigg|_{\Delta y=0} \left[\vec{\mathrm{x}}_o(y)\frac{d}{dy}\vec{\mathrm{z}}_e(y) - \vec{\mathrm{z}}_o(y)\frac{d}{dy}\vec{\mathrm{x}}_e(y)\right] \end{aligned} \tag{82}$$